

## Capillary flow in an interior corner

By MARK M. WEISLOGEL<sup>1</sup>† AND SETH LICHTER<sup>2</sup>

<sup>1</sup>NASA Lewis Research Center, M.S. 500/102, Cleveland, OH 44135, USA

<sup>2</sup>Department of Mechanical Engineering, Northwestern University, Evanston, IL 60208, USA

(Received 15 July 1997 and in revised form 8 June 1998)

The design of fluids management processes in the low-gravity environment of space requires an accurate description of capillarity-controlled flow in containers. Here we consider the spontaneous redistribution of fluid along an interior corner of a container due to capillary forces. The analytical portion of the work presents an asymptotic formulation in the limit of a slender fluid column, slight surface curvature along the flow direction  $z$ , small inertia, and low gravity. The scaling introduced explicitly accounts for much of the variation of flow resistance due to geometry and so the effects of corner geometry can be distinguished from those of surface curvature. For the special cases of a constant height boundary condition and a constant flow condition, the similarity solutions yield that the length of the fluid column increases as  $t^{1/2}$  and  $t^{3/5}$ , respectively. In the experimental portion of the work, measurements from a 2.2 s drop tower are reported. An extensive data set, collected over a previously unexplored range of flow parameters, includes estimates of repeatability and accuracy, the role of inertia and column slenderness, and the effects of corner angle, container geometry, and fluid properties. At short times, the fluid is governed by inertia ( $t \lesssim t_{Lc}$ ). Afterwards, an intermediate regime ( $t_{Lc} \lesssim t \lesssim t_H$ ) can be shown to be modelled by a constant-flow-like similarity solution. For  $t \geq t_H$  it is found that there exists a location  $z_H$  at which the interface height remains constant at a value  $h(z_H, t) = H$  which can be shown to be well predicted. Comprehensive comparison is made between the analysis and measurements using the constant height boundary condition. As time increases, it is found that the constant height similarity solution describes the flow over a lengthening interval which extends from the origin to the invariant tip solution. For  $t \gg t_H$ , the constant height solution describes the entire flow domain. A formulation applicable throughout the container (not just in corners) is presented in the limit of long times.

---

### 1. Introduction

The mechanism for capillary flows in interior corners is perhaps best introduced via an illustrative example. Figure 1 depicts a container with a square cross-section partially filled with a liquid in a strong gravitational field. Most of the interface is flat. However, as is commonly observed, especially in the corner regions of the container, the interface curves in order to satisfy the contact angle wetting condition along the perimeter of the interface. A magnified view of the corner region shows that the local radius of curvature  $R_i$  of the meniscus decreases as the corner is approached. Since the pressure drop across the meniscus is inversely proportional to  $R_i$  it follows that a pressure gradient along the corner is established in the wetting liquid. If gravity is suddenly ‘turned off’, the balance of this gradient with hydrostatic forces is disrupted

† Current address: TDA Research, 12345 W. 52nd Ave., Wheat Ridge, CO 80033, USA.

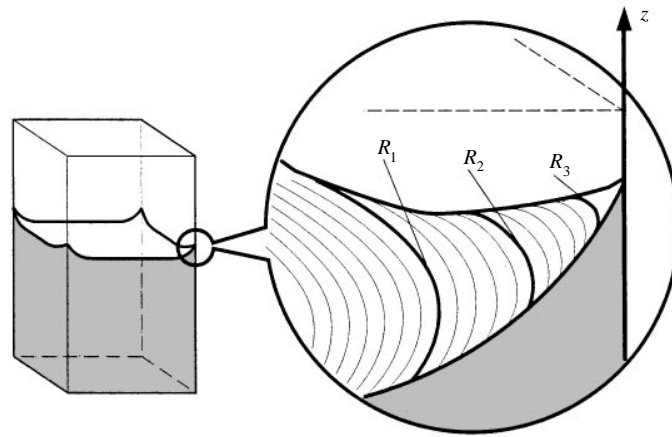


FIGURE 1. Partially filled square cross-sectioned container in 1-g.

and, as is illustrated in figure 2, slender columns rise as the fluid is pumped up the corners by capillary forces.

This work considers capillary flow along interior corners<sup>†</sup>, as a vessel's corners often provide the main conduit of capillary pumping under favourable wetting conditions. Such capillary pumping arises in numerous contexts and is particularly prevalent in low-gravity environments encompassing most, if not all, in-space fluids management processes, including the positioning, control, and transport of liquids, such as fuels in storage tanks, thermal systems such as heat pipes and capillary pumped loops, and the storage and handling of biological fluids and wastes (Jaekle 1991; Rollins, Grove & Jaekle 1985; Koster & Sani 1990). Examples of terrestrial applications include flows in porous media and the wetting and spreading of fluids on irregular surfaces – flow processes which are commonplace in nature and industry (Kistler 1993; Steen 1996).

The corner flow problem was recently studied by Dong & Chatzis (1995) who employed 0.3–0.5 mm diameter tubes of square cross-section in an analysis and experiment on imbibition as it relates to flows in porous media. Other relevant work was performed by Kolb & Cerro (1993), Legait (1983), Ma, Peterson & Lu (1994), and Singhal & Sommerton (1970). As in previous and related studies (Ransohoff & Radke 1988 and Ransohoff, Gauglitz & Radke 1987), it was assumed that the flow is locally parallel, and that streamwise curvature and inertia are negligible; the 'slow' flows and 'small' container size of these experiments provide an intuitive basis for such an approach. For a system of equivalent Bond number ( $Bo = \rho g H^2 / \sigma$ ) in a low-gravity environment, however, these assumptions come into question. For example, a measure of the influence of inertia in capillary-driven flows is provided by the Suratman number

$$Su = \sigma \rho H / \mu^2, \quad (1.1)$$

which is a Reynolds number based on the capillary velocity scale  $\sigma / \mu$ , where  $\mu$  is dynamic viscosity,  $\rho$  is density, and  $\sigma$  is interfacial tension. (Note that  $Su = Oh^{-2}$  where  $Oh$  is the Ohnesorge number.) A strong capillary presence is maintained when

<sup>†</sup> Interior corners are often referred to as grooves, edges, or wedges in the literature. A selection of pertinent references on capillary statics may be found in Concus & Finn (1990), Mason & Morrow (1991), Langbein (1990), and Wong, Morris & Radke (1992).

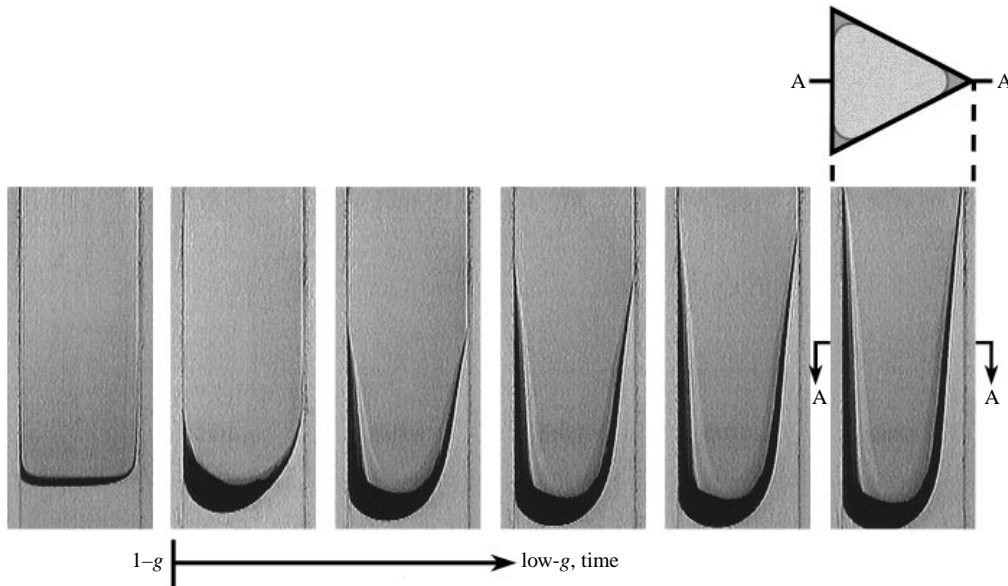


FIGURE 2. Selected frames from the cinefilm records of capillary rise in an equilateral triangle,  $D = 22.6$  mm, for 2.0 cS fluid at 0.2 s intervals (run LT2). The left-most frame in the sequence is at 1-g, with gravity downward. The subsequent five frames are during free-fall. A schematic of the top cross-sectional view of the cell is also shown. After nullification of the forces due to gravity, slender columns of fluid advance along the corners due to capillary forces. The retreating bulk meniscus takes the approximate form of a hemispherical cap.

the characteristic interfacial dimension  $H$  scales as the capillary length,  $H \lesssim (\sigma/\rho g)^{1/2}$ . Therefore,  $Su \sim (\sigma^3 \rho / \mu^4 g)^{1/2}$ . Thus, in a microgravity environment ( $g \sim 10^{-6} g_o$ , where  $g_o \doteq 9.812 \text{ m s}^{-2}$ ) the parametric range of  $Su$  is extended up to 3 orders of magnitude. Values of  $Su$  from low- $g$  experiments presented herein are  $\sim O(10^4)$  compared with similar normal-gravity tests by Dong & Chatzis (1995) where  $Su \sim O(1)$ . More dramatic yet are the changes which might be expected in the viscous time scale  $t_{visc} \sim \rho H^2 / \mu$ . With a 1000-fold increase of  $H$ , realizable in a low-gravity environment,  $t_{visc}$  increases by  $10^6$  over its normal-gravity counterpart! Increases in volumetric flow rate due to capillary pumping in a low- $g$  environment are expected to be similarly high.

Part of the difficulty in treating flow in corners is that the two-dimensional problem of flow through a wedge-shaped cross-section with a concave or convex free surface has no closed-form solution. The two-dimensional problem has been treated using finite elements and the flow resistance determined (Ayyaswamy, Catton & Edwards 1974; Ransohoff & Radke 1988). These tabulated values of the friction factor vary widely as a function of geometry; for example, they can take any positive value  $6 \lesssim \beta \lesssim \infty$ , where  $\beta$  is the dimensionless flow resistance determined by Ransohoff & Radke (1988). In the present work, the scaling incorporates the geometrical aspects of this dependence through a flow resistance coefficient  $F_i$ ; the remaining hydrodynamic contribution is a weak function of geometry and varies only within  $1/8 \lesssim F_i \lesssim 1/6$ . From such scaling, the interpretation of the geometrical effects are made obvious: for example, changes in contact angle affect the flow primarily by altering the driving pressure gradient (interface curvature) while changing the cross-sectional area only slightly, §3.4.

Emphasis is placed here on an asymptotic solution subject to the constraint that the interface height is constant at some location – a model for the ‘capillary rise’ problem introduced in figure 2. It has been found that utilizing this constraint as an upstream boundary condition yields good results for long times (Dong & Chatzis 1995). However, the use of this boundary condition is not self-evident and has lacked quantitative support, particularly for problems in which the initial transient plays a substantial role during the flow process, a characteristic of large-scale low-gravity flows. Experimental verification of this boundary condition as well as the asymptotic solutions, reproducibility and the influence of fabrication procedures is based on a large data set made possible by ready access to the drop tower at NASA’s Lewis Research Center.

In §2 the corner flow problem is formulated as a perturbation problem. Similarity solutions are presented in §3. For the central problem of this paper, that of capillary rise, we introduce the constant height boundary condition and show how the height can be computed from the shape of the equilibrium meniscus using the approach of de Lazzar *et al.* (1996). In §4–§5 experimental results for the capillary rise problem are compared with the similarity solution for  $Su$  in the range of 202 to 41 300. The formulation of a global similarity solution applicable throughout the container is introduced in §6. Finally, §7 summarizes the major results of the paper.

## 2. Formulation

Consider an isolated interior corner of angle  $2\alpha$  as depicted in figure 3. The corner is partially filled with a fluid making contact angle  $\theta$  with the solid surfaces and satisfying the Concus–Finn condition,  $\theta < \pi/2 - \alpha$ . (In their mathematical study, Concus & Finn (1969, 1974, 1990) were the first to obtain the result of the discontinuous behaviour of an interface in a corner at the critical value  $\theta = \pi/2 - \alpha$ ; when  $\theta < \pi/2 - \alpha$  the fluid spontaneously wicks into the corners. This condition appears also in heuristic studies concerning interfacial phenomena.) The  $z'$ -axis lies along the corner, and  $S'$  is the height of the free surface as measured from the  $(y', z')$ -plane. With  $L$  the characteristic length of the column of fluid along the  $z'$ -axis and  $H$  the characteristic height of the meniscus in the corner along the  $x'$ -axis, then  $\epsilon = H/L$  indicates the ‘slenderness’ of the flow geometry.

Table 1 provides the quantities used to non-dimensionalize the governing equations. Primes are used to denote dimensional dependent and independent variables. To the greatest extent possible, the scaling incorporates the flow geometry. The pressure is scaled using  $\sigma/Hf$ , where  $f^{-1} = (f(\alpha, \theta))^{-1}$  is a geometric function describing the curvature of the meniscus in the  $(x', y')$ -plane, to be defined later. This curvature scale holds when the curvature in the  $(x', z')$ -plane ( $\sim \partial^2 S'/\partial z'^2$ ) is small by comparison,  $\epsilon^2 f \ll 1$ . The characteristic  $z'$ -component of velocity,  $W$ , is determined through a balance of pressure and viscous forces and incorporates the geometric influence of  $\alpha$  and  $\theta$ .

The non-dimensionalized Navier–Stokes equations are to be solved together with the continuity equation in the form

$$A_t = -\dot{Q}_z = -(A\langle w \rangle)_z, \quad (2.1)$$

where  $A$  is the cross-sectional area of the flow in the  $(x, y)$ -plane,  $\dot{Q}$  is the volumetric flow rate in the  $z$ -direction, and  $\langle w \rangle \equiv \dot{Q}/A$ . A passive overlaying fluid is assumed and body forces are ignored.

The boundary conditions are the no-slip condition along the walls, the streamwise

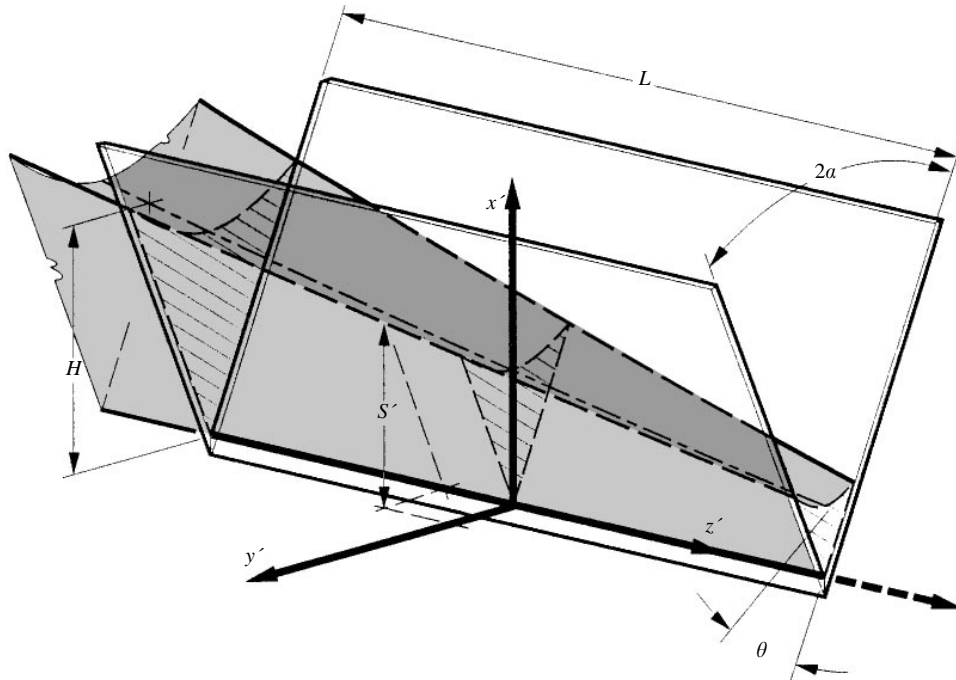


FIGURE 3. A fluid column in an isolated corner of angle  $2\alpha$ . The coordinate system is aligned such that the  $z'$ -axis is along the corner. The three-dimensional surface profile is given in terms of  $S'(y', z', t)$ . The characteristic height and length of the fluid column are  $H$  and  $L$ , respectively. The contact angle is  $\theta$ .

Lengths	Velocities	Other
$x = x'/H$	$u = u'/\epsilon W$	$P = HfP'/\sigma$
$y = y'/H \tan \alpha$	$v = v'/\epsilon W \tan \alpha$	$t = Wt'/L$
$z = z'/L$	$w = w'/W$	$A = A'/H^2 \tan \alpha$
$S = S'/H$	$\langle w \rangle = \langle w \rangle'/W$	$\dot{Q} = \dot{Q}'/WH^2 \tan \alpha$
$h = h'/H$	$W = \epsilon \sigma \sin^2 \alpha / \mu f$	
$\mathcal{L} = \mathcal{L}'/L$		

TABLE 1. Non-dimensionalized dependent and independent variables.

(confined to the  $(x, z)$ -plane) and transverse zero shear stress conditions on  $S$ , and the normal stress condition on  $S$ . Two additional boundary conditions on  $S$  are the meniscus centreline location and a symmetry condition on  $y = 0$ , namely

$$S = h \quad \text{on} \quad y = 0, \tag{2.2}$$

$$S_y = 0 \quad \text{on} \quad y = 0, \tag{2.3}$$

where  $h = h(z, t)$ . The remaining boundary conditions on  $S$  concern the treatment of the moving contact line. This poses particular difficulties in that the physics of the moving contact line is not fully understood due to the well-known stress singularity at the contact line itself (Dussan V. 1979; Kistler 1993). The simplest formulation of the

moving contact line boundary condition is the case of fluid statics where the condition

$$\mathbf{n} \cdot \mathbf{k} = \cos \theta \quad (2.4)$$

is applied. In (2.4),  $\theta$  is the static (or perhaps equilibrium) contact angle of the fluid-solid pair<sup>†</sup>,  $\mathbf{k}$  is the inward normal to the container walls (on  $y = \pm x$ ) given by  $\mathbf{k} = (\sin \alpha, \mp \cos \alpha, 0)$ , and  $\mathbf{n}$  is the outward unit normal to  $S$ . This boundary condition is strictly valid when  $\mathbf{v} = 0$  and may be approximately correct when the fluid velocity perpendicular to the contact line is small ( $Ca \equiv \mu U_{cl}/\sigma \ll 1$ ). This is, in general, the case for the corner flow problem discussed here where the predominant flow direction is parallel to the contact line. The net effect of applying (2.4) is to yield the two remaining boundary conditions for  $S$ , namely the slope and the location of the interface at the contact line, in terms of  $h$ . The inlet and outlet conditions at  $z = 0$  and  $z = 1$  and the initial conditions remain to be addressed.

### 2.1. Asymptotic equations

For the lubrication approximation,  $\epsilon^2 \ll 1$ , the dependent variables  $u, v, w, P$  and  $S$  are expanded in asymptotic series. Assuming  $\mathcal{R} \equiv (Su\epsilon^2 \sin^4 \alpha)/f \sim O(\epsilon^2)$ , the leading-order Navier–Stokes equations reduce to the single  $z$ -component equation

$$P_{oz} = w_{oxx} \sin^2 \alpha + w_{oyy} \cos^2 \alpha. \quad (2.5)$$

Also to leading order, the no-slip, shear and normal stress boundary conditions may be expressed as

$$\left. \begin{aligned} w_o &= 0 & \text{on } y = x, \\ w_{ox} - S_{oy} w_{oy} \cot^2 \alpha &= 0 & \text{on } x = S_o, \\ -P_o &= f S_{oyy} \cot^2 \alpha (1 + S_{oy}^2 \cot^2 \alpha)^{-3/2} & \text{on } x = S_o, \end{aligned} \right\} \quad (2.6)$$

where the transverse shear stress condition does not appear, as it is  $O(\epsilon)$ . The remaining boundary conditions are

$$w_{oy} = 0 \quad \text{on } y = 0,$$

$$S_o = h \quad \text{on } y = 0,$$

$$S_{oy} = 0 \quad \text{on } y = 0,$$

$$S_o = y_m \quad \text{on } y = y_m,$$

$$\frac{1 + S_{oy} \cot^2 \alpha}{(1 + S_{oy}^2 \cot^2 \alpha)^{1/2}} = \frac{\cos \theta}{\sin \alpha} \quad \text{on } y = y_m.$$

Noting that  $P_o = P_o(z, t)$ , the normal-stress equation (2.6) may be solved directly with its associated boundary conditions to find  $S_o$ ,  $y_m$ ,  $f$ , and  $P_o(h)$ . In this way the asymptotic analysis dictates that, to leading order, the fluid interface along the corner is a construct of circular arcs in planes parallel to the  $(x', y')$ -plane. Solutions to (2.6) and its associated boundary conditions are obtained by solving the geometrical ‘cross-flow’ problem sketched in figure 4 for the pressure in the liquid as a function of meniscus height  $h(z, t)$ , with the dimensional radius of curvature given by  $R' = fh'$

<sup>†</sup> If contact angle hysteresis is present and the contact line is in motion,  $\theta$  might best be taken as the advancing angle on first approximation. For a clear definition of the distinction between static and equilibrium contact angle and for a discussion of the difficulties faced when contact angle hysteresis is present in systems exhibiting partial wetting see Kistler (1993, p. 328).

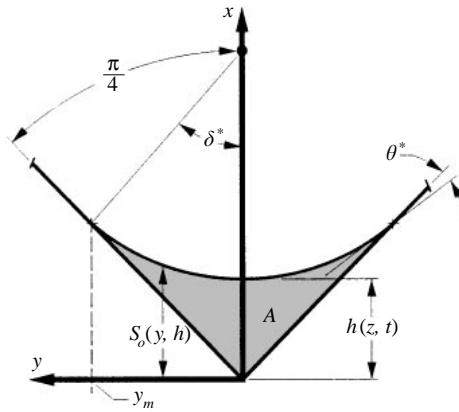


FIGURE 4. The dimensionless variables used in the cross-flow formulation (2.5)–(2.6). The height of the interface at a given  $z$  is  $S_o(y, h)$ , where  $h(z, t)$  is the height at  $y = 0$ . The contact line is located at  $y = y_m = hf \sin \delta \cot \alpha$ . When presented, as here, on the dimensionless  $(x, y)$ -plane, the contact angle  $\theta$  and the interface curvature angle  $\delta$  appear as  $\theta^* = \pi/4 - \tan^{-1}(\tan \alpha \tan \delta)$  and  $\delta^* = \sin^{-1}(\sin \delta \cot \alpha)$ .

(note that the curvature of the interface is not constant in the dimensionless  $(x, y)$ -plane). This yields

$$P_o = -1/h, \tag{2.7}$$

$$S_o = h(1 + f) - fh \left( 1 - (y \tan \alpha / fh)^2 \right)^{1/2}, \tag{2.8}$$

$$y_m = fh \sin \delta / \tan \alpha, \tag{2.9}$$

$$f = \left( \frac{\cos \theta}{\sin \alpha} - 1 \right)^{-1} = \left( \frac{\sin(\alpha + \delta)}{\sin \alpha} - 1 \right)^{-1}, \tag{2.10}$$

where  $\delta \equiv \pi/2 - \alpha - \theta$ . The angle  $\delta$  measures the degree of curvature of the interface in the  $(x, y)$ -plane.

The use of  $f$  in the non-dimensionalization of the problem leads to the simple expression for  $P_o$  given in (2.7) and the sign of  $f$  indicates either positive or negative curvature of the interface and thus the anticipated flow direction of the  $z$ -component velocity. Positive curvature is depicted in figure 4, and  $f \geq 0$  for systems satisfying the Concus–Finn condition. The parameter  $f$  characterizes the strength of the driving force for the flow due to curvature of the interface, independent of the cross-flow area. The parameter  $F_A = F_A(\alpha, \delta)$  is the cross-sectional area function ( $A' = h^2 F_A$ ) and may be determined geometrically,

$$F_A = \frac{f^2 \sin^2 \delta}{\tan \alpha} \left( 1 - \left( \frac{2\delta - \sin 2\delta}{1 - \cos 2\delta} \right) \tan \alpha \right). \tag{2.11}$$

Figure 5 shows  $F_A$  and  $f$  plotted against  $\delta$  for a variety of corner half-angles  $\alpha$ . Note that  $F_A$  shows only weak functional dependence on  $\delta$  for fixed  $\alpha$ , and that for all  $\alpha$  and  $\delta$ ,  $1 \leq F_A / \tan \alpha \lesssim 4/3$ . Note also that  $f$  behaves like  $1/\delta$  for  $\delta \rightarrow 0$ .

Regardless of the technique employed to solve (2.5), the resulting form for  $\langle w_o \rangle$  is

$$\langle w_o \rangle = -F_i h^2 P_{oz} = -F_i h_z, \tag{2.12}$$

where  $F_i$  is a positive geometric function of  $\alpha$  and  $\delta$ . Viscous resistance ( $\sim h^{-2}$ ) is

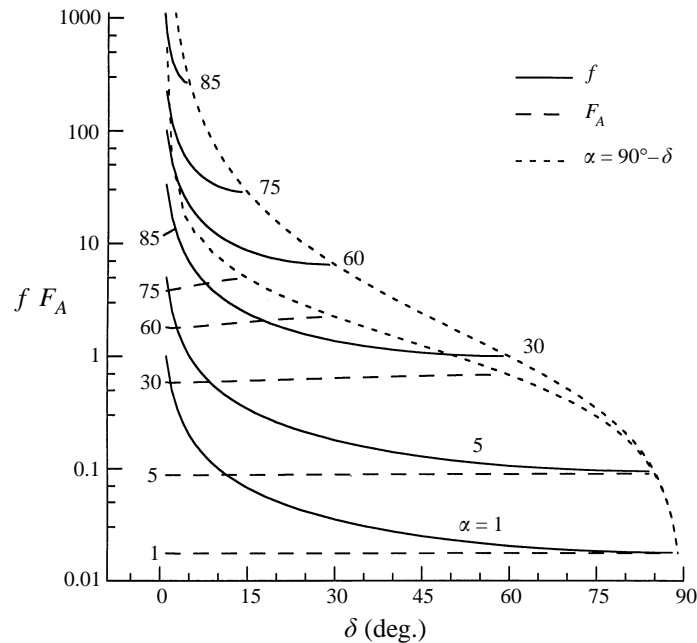


FIGURE 5. The parameters  $f$  and  $F_A$  as a function of  $\delta \equiv \pi/2 - \alpha - \theta$  for various  $\alpha$  (deg.).  $f^{-1}$  indicates the strength of the capillary driving force. For given centreline height,  $F_A$  is proportional to the dimensional cross-sectional area of the flow.

balanced by capillary forces ( $\sim h^{-2}h_z$ ) in such a way as to leave  $\langle w_o \rangle$  dependent only on the slope of the interface  $h_z$ , and not on  $h$ . As a result, non-zero velocities are possible for  $h \rightarrow 0^+$  provided  $h_z \neq 0$ .

Noting that  $A \propto h^2$  (2.12) is substituted into (2.1) yielding

$$2h_t = F_i (2h_z^2 + hh_{zz}). \quad (2.13)$$

We now turn to evaluating the coefficient  $F_i$ .

## 2.2. Flow resistance, $F_i$

Generally speaking, Ransohoff & Radke (1988) and Ayyaswamy *et al.* (1974) have determined  $F_i$  for this problem.† They first use a finite element scheme to solve (2.5) for  $w_o$ . They then integrate over the cross-sectional area to determine  $\langle w_o \rangle$  and tabulated results are presented in terms of either a dimensionless flow resistance,  $\beta$ , in the case of Ransohoff & Radke, or a dimensionless friction factor coefficient,  $K$ , as in the case of Ayyaswamy *et al.* Also, Ransohoff *et al.* (1987) employ the continuity equation in the general form of (2.13) to numerically solve for a problem relating to snap-off in constricted pores, while Dong & Chatzis (1995) find a similarity solution applicable to imbibition in square capillary tubes. The usefulness of these solutions is that they are only restricted to  $\epsilon^2 \ll 1$  (slender fluid column),  $\epsilon^2 f \ll 1$  (slight curvature along  $z$ -axis), and  $\mathcal{R} \sim O(\epsilon^2)$  (small inertia). For many practical systems  $f \sim O(1)$  and the second constraint is satisfied by the first. The tabulated values of  $\beta$  and  $K$  vary over a wide range. However, much of this variation can be consumed

† Lenormand & Zarcone (1984) and L. Trefethen (unpublished, 1990) use a hydraulic diameter approach in effect to determine  $F_i$ , the utility of which is discussed in Ransohoff & Radke (1988).



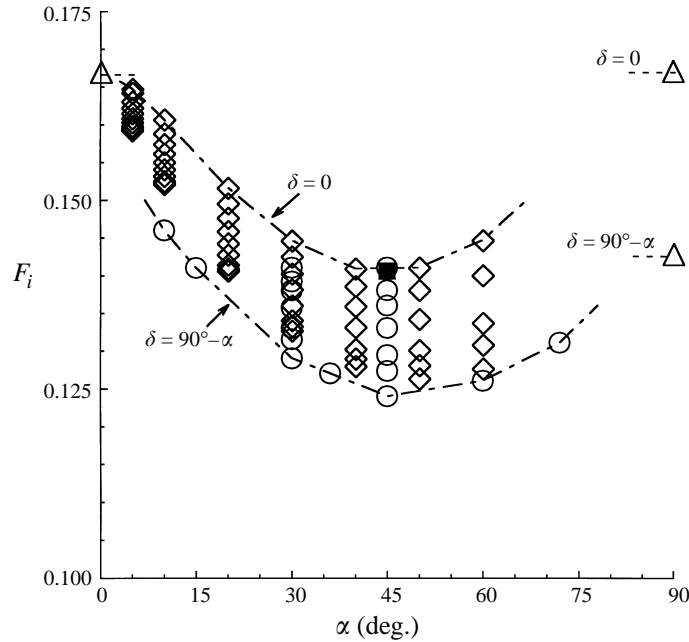


FIGURE 6. The flow resistance,  $F_i(\alpha, \theta)$ . The value of  $F_i$  falls between the curves for  $\delta = 0$  and  $\delta = \pi/2 - \alpha$  (i.e.  $\theta = 0$ ) approximated by dashed lines from the data of Ransohof & Radke (1988) ( $\circ$ ) and Ayyaswamy *et al.* (1974) ( $\diamond$ ). With the scaling introduced in table 1, it is seen that for all  $\alpha$  and  $\delta$ ,  $1/8 \lesssim F_i \lesssim 1/6$ . The dotted lines emanating from  $\triangle$  show the asymptotic approximations valid in the limits of small ( $F_I$ ) and large ( $F_{II}$ )  $\alpha$ , as determined in the Appendix;  $\blacksquare$  is from an exact solution ( $F_{III}$ ) for  $\alpha = \theta = \pi/4$ , also given in the Appendix.

through scaling. Furthermore, under certain restricted conditions, once scaled, it is possible to find analytic forms for the flow resistance  $F_i$ .

From the definition of  $\beta$ , it can be shown that  $F_i = f^2/\beta \sin^2 \alpha$ . Though the tabulated values of  $\beta$  yield a semi-infinite range of values  $6 \lesssim \beta \lesssim \infty$  for the full range of  $\theta$  and  $\alpha$  satisfying the Concus–Finn condition,  $F_i$  varies only slightly  $1/8 \lesssim F_i \lesssim 1/6$ , see figure 6. Ayyaswamy *et al.* (1974) considered gravity-driven capillary flow in triangular grooves and calculated a friction factor coefficient  $K$ . It can be shown that  $F_i = 8 (F_A/f \sin \delta)^2 / K$ . Over the range of tabulated values  $5^\circ \leq \alpha \leq 60^\circ$  and  $0 \leq \delta \leq 84.9^\circ$  it is found that  $30 \lesssim K \lesssim 57$ . However, while  $K \sim O(10)$ , note that  $F_i \sim O(1)$  and the variation of  $F_i$  is considerably less than that of  $K$ . Thus the characteristic quantities introduced in table 1 appropriately scale the governing equations; in particular  $1/\sin^2 \alpha$  and  $1/f$  appearing in  $W$  capture the respective geometric components of viscous resistance and capillary driving force for the flow.

For the limiting cases of small and large corner half-angle  $\alpha$ , asymptotic techniques yield an approximate value for the flow resistance  $F_i$ . In addition, an exact analytic expression for  $F_i$  is possible for the special cases of  $\theta = \alpha = \pi/4$ . These solutions are presented in the Appendix and the results are shown on figure 6. Solutions for  $F_i$  for liquids with large surface viscosity are presented in Weislogel (1996).

With  $F_i$  determined from numerical or analytical techniques (2.13) is transformed into the governing partial differential equation

$$h_\tau = 2h_z^2 + hh_{zz}, \tag{2.14}$$

where  $\tau = F_i t/2$ . Gravity acting along the  $x$ -direction,  $g_x$ , may be considered by modifying the pressure gradient such that  $P_{o_z} = (h^{-2} + Bo_H) h_z$ , where  $Bo_H = f \rho g_x H^2 / \sigma$  is the Bond number based on surface curvature (via  $f$ ). A pressure gradient (e.g. gravity) acting along the  $z$ -direction leads to an additional term in (2.14) which if included would recover the foam drainage equation recently reviewed by Verbist, Weaire & Kraynik (1996) and applied to the corner flow problem by Kovscek & Radke (1996).

### 3. Similarity solutions

In this section the generalized similarity ODE for  $h(z, t)$  is introduced. Solutions applicable to the special cases of a constant height boundary condition and a constant inlet flow condition are reviewed. Such solutions serve as models for the spontaneous flows of capillary rise and a constant flow rate, respectively, as will be discussed. Other solutions are only briefly discussed as they can be found in the literature (see Mayer, McGrath & Steele 1983 where related solutions are presented in the context of nonlinear heat conduction, and Barenblatt & Zel'dovich 1972 for an earlier review). All of the cases considered possess an advancing meniscus at the tip. The location of the tip on the  $z$ -axis is denoted by  $\mathcal{L} = \mathcal{L}(\tau)$ , where  $h(\mathcal{L}, \tau) = 0$  is assumed.

The introduction of

$$h = \tau^a F(\eta), \quad \eta = |b|^{1/2} z \tau^b, \quad \mathcal{L} = \eta_{tip} |b|^{-1/2} \tau^{-b}, \quad (3.1)$$

leads to similarity in (2.14) when  $b = -(1+a)/2$ . By further noting that the result is invariant under the transformation  $F = \lambda^2 F^+$  and  $\eta = \lambda \eta^+$ , the common requirement of  $h(\mathcal{L}, \tau) = F(\eta_{tip}) = F^+(\eta_{tip}^+) = 0$  for problems involving an advancing tip permits the determination of the slope at the tip, namely  $F_{\eta^+}^+(\eta_{tip}^+) = -\eta_{tip}^+ / 2$ . Due to the added degree of freedom introduced by  $\lambda$  it is convenient to set  $\eta_{tip}^+ = 1$ . When numerical solution is necessary, knowing both  $F^+$  and  $F_{\eta^+}^+$  at the tip allows a single-step backwards Runge–Kutta method. The parameter  $\lambda$ , and hence  $F$  and  $\eta$ , can then be determined by the applicable boundary condition or integral constraint. Equation (2.14) thus transforms to the invariant similarity equation

$$F^+ F_{\eta^+ \eta^+}^+ + 2F_{\eta^+}^{+2} + \eta^+ F_{\eta^+}^+ - \frac{2a}{1+a} F^+ = 0, \quad (3.2)$$

subject to  $F^+(1) = 0$  and  $F_{\eta^+}^+(1) = -1/2$ .

Figure 7 presents solutions to (3.2). Solutions do not intersect the positive  $F^+$ -axis for  $a < -1/3$ . For  $a = 1$  a linear solution  $F^+ = (1 - \eta^+)/2$  holds. Furthermore, the linear solution is the asymptote for all  $a$  as  $\eta^+ \rightarrow 1$ .

The difficulty now faced is one of identifying practical boundary conditions. This can be accomplished by assuming that the dimensional volume  $Q'$  of fluid in the corner  $\eta^+ \geq 0$  is  $Q' \propto t^m$ . The condition for similarity which now reads  $5a + 1 - 2m = 0$ , leads to an integral volume constraint on the volume of fluid flow into the corner  $\eta^+ \geq 0$ ,

$$\lambda^5 \left( \frac{2}{|1+a|} \right)^{1/2} \int_0^1 F^{+2} d\eta^+ = k_m, \quad (3.3)$$

where  $k_m = k'_m (2L/F_i W)^m / F_A H^2 L$  and  $k'_m$  is a constant. Recall (e.g. from (2.12)) that a positive (negative) slope of the curves in figure 7 indicates flow in the negative (positive)  $\eta^+$ -direction. So, for  $m < 0$  ( $-1/3 \leq a < -1/5$ ) the volume within the

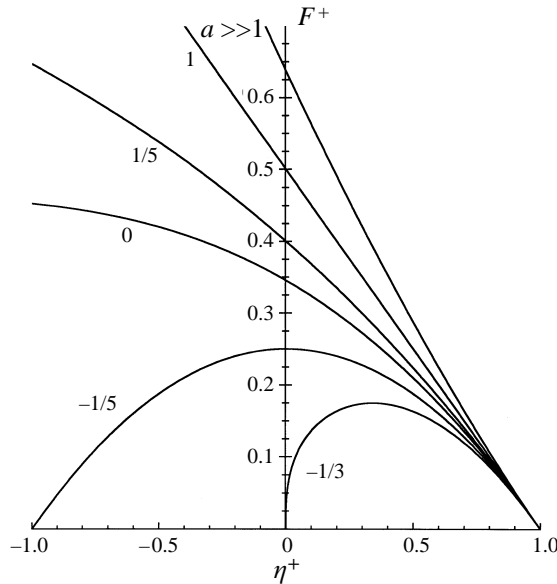


FIGURE 7. Similarity function  $F^+(\eta^+)$ . For the capillary rise problem discussed in §3.1  $a = 0$ . A drop spreading along the corner is described by  $a = -1/5$ ; the constant flow rate boundary condition corresponds to  $a = 1/5$ , and exponential flow rate to  $a \gg 1$ . For  $a = 1$ ,  $F^+(\eta^+)$  is linear. Solutions for all values of  $a$  are asymptotic to the linear solution as they approach the tip  $\eta^+ = 1$ .

corner is decreasing due to removal of fluid at the origin. For  $m > 0$  ( $a > -1/5$ ) there is inflow at the origin.

3.1. Constant height condition (capillary rise)

Consider an initially flat interface ( $Bo_i \gg 1$ ) in the  $(x, y)$ -plane. Gravity, acting in the negative  $z$ -direction, is suddenly ‘turned off’ and the flow proceeds up the corner in the positive  $z$ -direction due to capillary forces (as in figure 2). The choice of  $a$  and  $b$  for this problem is not obvious. In §4, it is shown that there is a  $z$ -location such that the interface height is constant for long enough times. This height is approximated by de Lazzar *et al.* (1996) who determine the shape of static menisci in polygonal cylinders. Given the value of the curvature of the free surface, there is an equilibrium value for the pressure jump across the free surface. Here, it is assumed that at the  $z$ -location which *locally* satisfies the equilibrium condition, the interface height is steady. Then, the *dimensional* height  $H$  for rectangular cross-sectioned cylinders of dimensional face widths  $D_i$  is

$$H_{rect} = \frac{jD_2 \sin(\alpha + \delta)}{4f \frac{F_{\bar{A}}}{F_{\bar{A}}}} \left[ 1 - \left( 1 - \frac{D_1}{D_2} \frac{4F_{\bar{A}}}{j^2 \sin^2(\alpha + \delta)} \right)^{1/2} \right], \tag{3.4}$$

and for  $n$ -sided regular-polygons of face width  $D$  it is

$$H_{n-poly} = \frac{D \sin(\alpha + \delta)}{2f \frac{F_{\bar{A}}}{F_{\bar{A}}}} \left[ 1 - \left( 1 - \frac{F_{\bar{A}} \cot \pi/n}{\sin^2(\alpha + \delta)} \right)^{1/2} \right] \equiv F_H D, \tag{3.5}$$

where  $\delta = \pi/n - \theta$ ,  $\alpha = \pi(n-2)/2n$ ,  $j = 1 + D_1/D_2$  and  $F_{\bar{A}} = \sin^2 \delta / \tan \alpha + \sin \delta \cos \delta - \delta$ . From (3.4), for variations of the aspect ratio  $0 \leq D_1/D_2 \leq 1$ , it can be shown that

§	Flow	$a$	$\eta_{tip}$	$F_\eta(\eta_{tip})$	$F(0)$	$F_\eta(0)$
3.1	Const. height	0	1.702	-0.851	1	-0.349
3.2	Const. flow	1/5	$1.917q^{1/5}$	$-0.958q^{1/5}$	$1.470q^2/5$	$-0.598q^{1/5}$
3.3	Const. vol.	-1/5	$1.801\kappa^{1/5}$	$-0.901\kappa^{1/5}$	$0.811\kappa^{2/5}$	0
3.3	Exp. flow	$\gg 1$	1.252	-0.626	1	-0.481
3	Linear profile	1	1.644	-0.822	1.351	-0.822

TABLE 2. As described in the sections indicated, solutions to (3.2) describe different types of flows, as set by the similarity parameter  $a$ . In terms of the similarity variables, the position  $\eta_{tip}$  and slope  $F_\eta(\eta_{tip})$  of the tip of the fluid column and the height  $F(0)$  and slope  $F_\eta(0)$  at the origin are given.

$1/2 \lesssim Hf \cos \theta / D_1 \lesssim 1$ , and so the effect of aspect ratio is weak. In §4 we compare the predicted height  $H_{3-poly}$  with experimental measurement.

Based on the above considerations it is conjectured that for  $\tau > \tau_H$  there exists a location  $z_H$  such that the interface height  $h(z_H, \tau)$  remains constant. With no loss of generality, the location of  $z_H$  is transferred to the origin  $z = 0$  and  $h(0, \tau) = 1$ . To satisfy this condition it is necessary to choose ( $m = 1/2$ ). The numerical solution to (3.2) is shown in figure 7 ( $a = 0$ ) and gives  $F^+(0) = 0.345\dots$  and  $F_{\eta^+}^+(0) = 0.205\dots$ . The location and slope of the interface at the tip, and the height and slope of the interface at  $\eta = 0$  are determined and listed in table 2 as  $\eta_{tip}$ ,  $F_\eta(\eta_{tip})$ ,  $F(0)$ , and  $F_\eta(0)$ , respectively.

### 3.2. Constant inlet flow rate

When the flow rate  $q$  at the inlet ( $z = 0$ ) is held fixed, the amount of fluid in the corner increases linearly with time ( $m = 1$ ). The integral mass balance of (3.3) demands  $a = 1/5$  and yields

$$\lambda^5 (5/3)^{1/2} \int_0^1 F^{+2} d\eta^+ = 2q, \quad (3.6)$$

where  $q$  is the prescribed dimensionless constant flow rate at  $\eta = 0$ . Numerical solution of (3.2) for  $a = 1/5$  gives  $F^+(0) = 1.400\dots$  and  $F_{\eta^+}^+(0) = -0.312\dots$  and is presented graphically in figure 7.

### 3.3. Other solutions

Additional similarity solutions are available for analyses of corner flows: the condition  $a = -1/5$  ( $m = 0$ ) models a drop of volume  $H^3$  (dimensionless drop volume  $\kappa = \epsilon/2F_A$ ) spreading symmetrically about  $\eta^+ = 0$ . For this choice of  $a$  (3.2) is solved analytically to yield  $F^+ = (1 - \eta^{+2})/4$  from which the entire three-dimensional surface may be expressed explicitly. The detailed character of this solution along with experimental verification as it relates to the practical problem of a spreading drop is given in Weislogel & Lichter (1996). A solution for exponential increase in  $h(0, \tau)$  is also possible (Marshak 1958) and is modeled by (3.2) in the limit  $a \gg 1$ . The *dimensional* result for  $h(z, t)$  is  $h = h_o F(\eta) \exp[rt]$ , where  $r$  (in  $s^{-1}$ ) is the rate exponent. These solutions are included in figure 7 and useful numerical quantities for these cases are in table 2.

### 3.4. Geometric effects

The dependence of the flow on geometry is well accounted for within the scaling. This is best seen from the dimensional form of the results. For the similarity solutions

§	Flow	$a$	$\mathcal{L}(t)$	$\dot{Q}(0, t)$
3.1	Const. height	0	$1.702G^{1/2}H^{1/2}t^{1/2}$	$0.349F_A G^{1/2}H^{5/2}t^{-1/2}$
3.2	Const. flow	1/5	$1.634(F_A^{-1}\dot{Q})^{1/5}G^{2/5}t^{3/5}$	$\dot{Q}$
3.3	Const. vol.	-1/5	$1.879F_A^{-1/5}G^{2/5}H^{3/5}t^{2/5}$	0
3.3	Exp. flow	$\gg 1$	$1.252(h_0G/r)^{1/2}\exp[rt/2]$	$0.306F_A h_0^{5/2}(rG)^{1/2}\exp[5rt/2]$
-	Linear flow	1	$0.822\epsilon Gt$	$0.375\epsilon^5 F_A G^3 t^2$

TABLE 3. Dimensional (primes dropped) tip location  $\mathcal{L}(t)$  and flow rate  $\dot{Q}(0, t)$  at the origin for the similarity solutions derived in the subsections shown.  $G \equiv \sigma F_i \sin^2 \alpha / \mu f$ .

discussed above, table 3 lists the dimensional tip location and flow rate, where  $G \equiv \sigma F_i \sin^2 \alpha / \mu f$ .

Considering the case of the constant height boundary condition and recalling that  $F_i$  varies only slightly, it can be shown that in  $n$ -sided polygons, for  $\delta \ll 1$  with  $\alpha$  fixed,  $\mathcal{L} \sim 1/f$ . Since  $f$  is a direct measure of the driving pressure gradient, the effect of increasing contact angle, or equivalently the limit  $\delta \rightarrow 0$ , should be seen as impacting the tip location  $\mathcal{L}$  by reducing primarily the driving pressure gradient through  $f$  as opposed to the cross-sectional area for flow. This is also true for the flow rate  $\dot{Q} \sim G^{1/2}H^{5/2}$ . This explanation holds true for each of the flow scenarios solved herein.

As can be easily computed from table 3, the spreading rate is maximized when  $\theta = 0$ ,  $\alpha \simeq 17^\circ$  for the constant flow rate and constant volume problems. For the constant height and exponential flow rate solutions the rate is maximized when  $\theta = 0$ ,  $\alpha \simeq 30^\circ$ .

#### 4. Capillary rise experiments

This section describes experiments on the capillary rise of a liquid in an interior corner in a low-gravity environment. Digitized surface traces of the developing flow are compared with the analytical results of the preceding section. Additional experiments conducted to quantify the broader effects of corner angle, container size, interior surface conditions, and a wide range of fluid properties including system contact angle will be described in a subsequent publication.

##### 4.1. Introduction to low-g experimentation

Experimentation in a low-gravity environment is unique in several respects. Capillary flows can be orders of magnitude larger than their normal-gravity counterparts. The large cell size, in addition to extending the range of certain fluid parameters, also allows greater precision in container fabrication, diminishing the role of surface contamination through corner irregularity and roundedness, surface roughness, and other heterogeneities.

A 2.2 second drop tower test facility at NASA's Lewis Research Center is used to access the low-g environment for the capillary rise tests. Though the low-g time afforded by the drop tower is limited, the cells tested are sized to make adequate use of the time available. The drop tower is approximately 27 m in height. Gravity levels of  $10^{-4}g_0$  are common. A detailed description of this facility may be found in Lekan *et al.* (1996). The description here is restricted to the test/drop rig apparatus.

$\nu \pm 2\%$ (cS)	$\rho \pm 5$ ( $\text{kg m}^{-3}$ )	$\sigma \pm 5\%$ ( $\text{N m}^{-1}$ )	$N_D$
0.65	760	0.0159	1.374
1.0	816	0.0174	1.383
2.0	872	0.0187	1.390
5.0	913	0.0197	1.396
10.0	935	0.0201	1.399
20.0	949	0.0206	1.399

TABLE 4. Test fluids and properties. Polydimethylsiloxane (PDMS, silicone oil) provided by Dow Corning. The static contact angle  $\theta_{stat} = 0$  on all surfaces. The kinematic viscosity, density, and surface tension are denoted by  $\nu$ ,  $\rho$ , and  $\sigma$ , respectively. The refractive index is  $N_D$ .

Cell cross-section (section type)	$D$ or $D_1 \times D_2$ ( $\pm 0.05$ mm)	$\alpha$ (deg.)
equil. triangle	12.0	30
equil. triangle	22.6	30
near square	$6.1 \times 6.7$	45
near square	$12.9 \times 13.2$	45
rectangle	$6.0 \times 13.0$	45
rectangle	$6.1 \times 25.6$	45

TABLE 5. Acrylic test cell data for capillary rise tests. The refractive index is  $N_D = 1.491$ , the total length of the cell is 150 mm, the corner half-angle is  $\alpha$ , and, for cross-sectional shapes in which the face widths are equal (unequal), the face widths are  $D$  ( $D_1, D_2$ ).

#### 4.2. Description of the experiment

A transparent test cell is installed in a drop rig apparatus. Prior to release of the apparatus into free fall, a prescribed amount of fluid is injected into the cell, partly filling it. Upon release, hydrostatic forces are essentially eliminated and capillary-driven flow results. As fluid is drawn downstream along the corners, the fluid near the container centreline bows forming the ‘bulk meniscus’ which recedes upstream. The flow process is backlit by a diffuse light source and filmed at a long working distance with a high-speed cine-camera at 128 frame/s. A sample of frames at 0.2 s intervals taken from the film records is provided as figure 2 for 2.0 cS silicone oil fluid (PDMS) in a 22.6 mm equilateral triangular cell. Quantitative data are digitized directly from the film records.

The principle variables for the drop tests are the container face width  $D$  and fluid viscosity  $\mu$ . Corner half-angle  $\alpha$  and liquid–solid contact angle  $\theta_{stat}$  are also parameters of interest, but in this report only systems with  $\theta_{stat} = 0$  will be considered. The properties of the liquids and test cells for the tests to be presented are listed in tables 4 and 5, respectively.

The physical condition of the corner is critical for such flows. Figure 8 displays the joining technique of the faces of the cells. These cells are fused at the joints. In order to assess fabrication variability, two of each cell were constructed.

The majority of the tests are performed using cells of square or equilateral triangular cross sections, figures 8(a,b). For both of these configurations, the cells are fabricated such that the meniscus centreline along the corner  $h(z, t)$  can be viewed in profile with a minimum of optical distortions. A ray trace analysis which provides corrections for distortion due to mismatch of the refractive indices is employed for certain

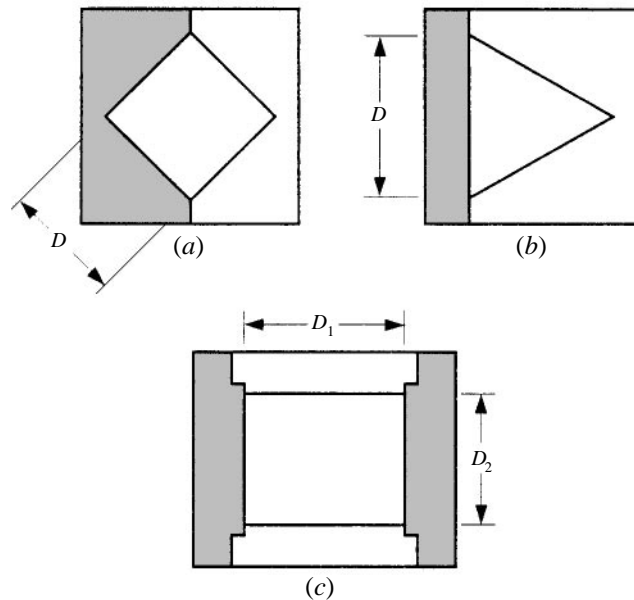


FIGURE 8. Cross-sections of capillary rise test cells. The square (a) and equilateral triangular (b) cross-sections were constructed of two pieces of acrylic, while the rectangular cross-sections (c) used four pieces.

measurements. These corrections are never greater than 10% in the measured value of  $h(z, t)$  and in most cases are  $\lesssim 3\%$ .

Cell preparation includes washing with a soap solution in hot water, rinsing thoroughly with distilled water, then rinsing with ethanol and/or methanol followed by a final distilled water rinse. The cells are allowed to air dry or are dried in a vacuum oven.

#### 4.3. Tip location, $\mathcal{L}(t)$

The principal measured quantities from the film records are the location of the leading tip of the fluid in the corner  $\mathcal{L}(t)$  and the height along the centreline,  $h(z, t)$ , see figure 4. (Measured quantities are presented dimensionally unless otherwise specified, all length measurements are in mm.) A sample of results for  $\mathcal{L}(t)$  is provided here, while a comprehensive analysis of  $h(z, t)$  for several data sets is deferred to §4.4. Figures 9–11 made using a film motion analyser in manual mode without image processing, are intended to convey the general character of the flow.

Figure 9 displays data on the effect of viscosity on the tip location  $\mathcal{L}(t)$  for tests performed in an equilateral triangular section container with  $D = 12.0$  mm. As suggested by table 3, data for different values of the viscosity collapse onto a single line by using the parameter  $(\sigma t / \mu)^{1/2}$ . As anticipated, the tip velocity increases with decreasing viscosity and increasing cell size as also observed by Dong & Chatzis (1995). Figure 10 shows the impact of cell size and corner angle on the tip location for a fluid of fixed viscosity. The 22.6 mm triangle (12.0 mm triangle) has approximately the same inscribed circle radius as the 12.9 mm near-square (6.1 mm near-square). The collapse of the data with  $(F_i H t \sin^2 \alpha / f)^{1/2}$  is favourable. When the raw unscaled data are viewed, it can be seen that the tip velocity is greater for  $\alpha = 30^\circ$  compared to  $\alpha = 45^\circ$ , as indicated by the scaling, §3.4. Figure 11 illustrates the effect of container

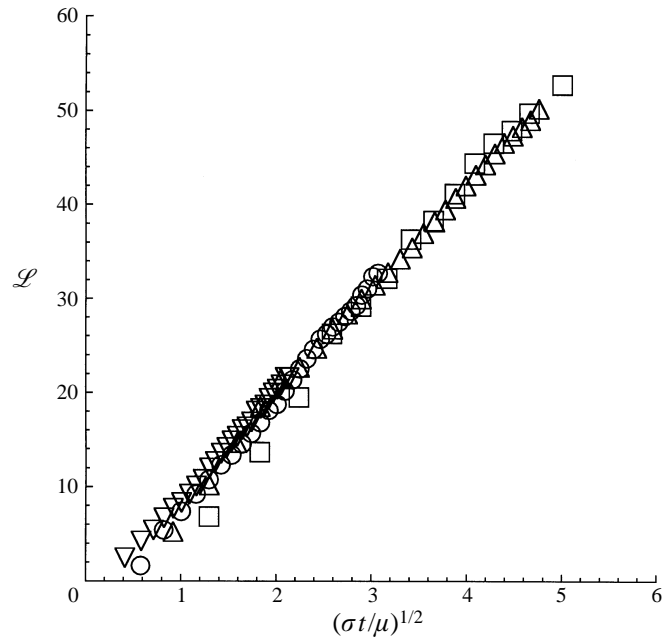


FIGURE 9. The location of the tip of the fluid column  $\mathcal{L}$  (mm) as a function of  $(\sigma t/\mu)^{1/2}$  ( $\text{m}^{1/2}$ ) in the equilateral triangle with  $D = 12.0$  mm for fluids of different viscosity:  $\square$ , 1.0;  $\triangle$ , 2.0;  $\circ$ , 5.0;  $\nabla$ , 10.0 cS.

aspect ratio for rectangular cross-sectioned cells and fixed fluid properties, as described by (3.4).

Multiple drop tests are made to note the repeatability of the measurements in regard to cleaning technique, fill technique, etc. Each test was performed up to 18 times. The majority of tests show repeatability to within  $\pm 6\%$  when comparing fitting parameter coefficients for the different runs and  $\pm 3\%$  is common. With this level of precision it is easy to quantify differences in flow behaviour from vessel to vessel, and even from corner to corner of the same vessel. Concerning the latter, as regards the tip location, asymmetric flows are detected between different corners of the same vessel. These differences are repeatable (again to within  $\pm 6\%$ ) and are assumed to be linked to discrepancies in the fabrication quality of the corners. The largest differences are observed in the tip location measurements for the rectangular cross-section vessels, yet are always less than 10%.

When the Concus–Finn condition is satisfied, regardless of the gravity level, a thin column of fluid already exists in the corner prior to the drop test (Concus & Finn 1974*b*). This pre-existing film makes ambiguous the true tip location of the meniscus during the early stage of the drop tests. An apparent  $\mathcal{L}(t)$  was thus measured at the onset of the flow by extrapolating the apparently linear meniscus profile near the tip to the vertex of the corner. As the fluid column rises, upper portions of the corners are reached where the film is not observed and data taken in these regions needs no extrapolation.

Another complication in the tip measurements is that during the latter stages of the corner flow the tip location for some of the tests (usually low-viscosity fluids in the smaller test cells) becomes increasingly difficult to locate as the slope of the



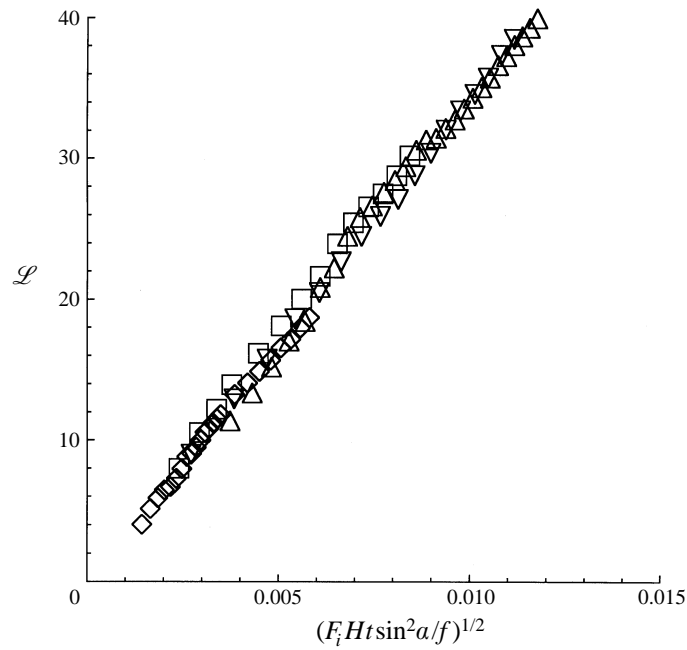


FIGURE 10. The tip location  $\mathcal{L}$  (mm) as a function of  $(F_i H t \sin^2 \alpha / f)^{1/2}$  ( $(\text{m s})^{1/2}$ ) illustrating the effect of cell size and corner angle for a wetting fluid of kinematic viscosity 5.0 cS.  $\triangle$ ,  $D = 22.6$  mm triangle;  $\nabla$ , 12.0 triangle;  $\square$ , 12.9 near square; and  $\diamond$ , 6.1 near square. The fluid rises fastest when the cross-sectional shape is an equilateral triangle,  $\alpha = 30^\circ$ .

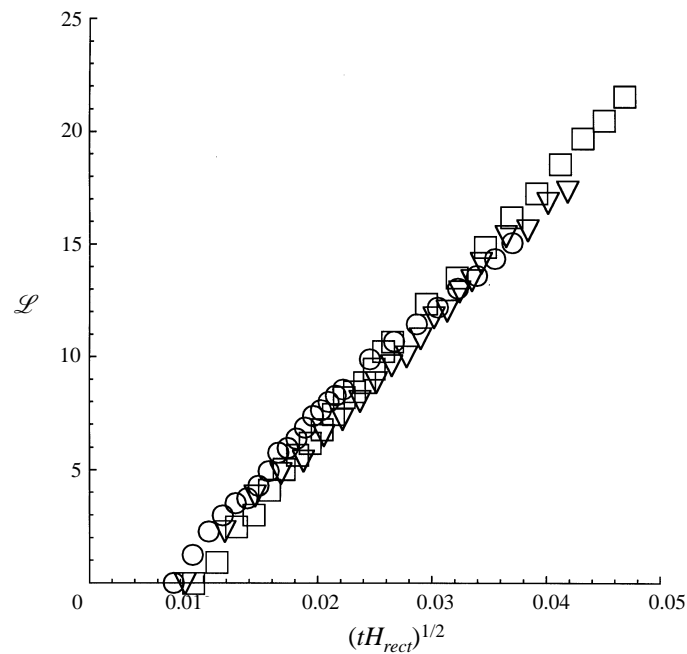


FIGURE 11. The tip location  $\mathcal{L}$  (mm) as a function of  $t^{1/2}$  ( $\text{s}^{1/2}$ ) in rectangular cells for a fluid of  $\nu = 5.0$  cS showing the effect of aspect ratio.  $\circ$ ,  $D_1 \times D_2 = 6.1 \times 6.7$  mm,  $\nabla$   $6.0 \times 13.0$ ; and  $\square$ ,  $6.1 \times 25.6$ . As expected from (3.4), aspect ratio has only a weak effect.

Test	$Su$ ( $\rho\sigma H/\mu^2$ )	$D$ (mm)	$\nu$ (cS)	$t_H$ (s)	$H_{exp}$ (mm)	$H_{3-poly}$ (mm)	$t_\epsilon$ ( $\times 100$ s)	$t_{visc}$ (s)	$t_{\epsilon R}$ (s)
ST1	41 300	12.0	1.0	0.25	$1.80 \pm 0.09$	1.94	0.009	0.47	0.17
ST10	417	12.0	10.0	0.4	$1.97 \pm 0.08$	1.94	0.09	0.047	1.7
LT2	20 000	22.6	2.0	0.4	$3.73 \pm 0.15$	3.67	0.32	0.84	0.65
LT20	202	22.6	20.0	1.0	$3.70 \pm 0.14$	3.67	3.2	0.084	6.5

TABLE 6. Data for capillary rise tests for a range of Suratman numbers in small  $D = 12.0$  mm and large  $D = 22.6$  mm equilateral triangular containers. For  $t > t_H$  the constant height condition is established.  $H_{exp}$ , the measured value of the constant height  $h(z_H, t > t_H)$ , compares well with  $H_{3-poly}$ , which is calculated from (3.5). The time constants associated with satisfying the assumptions of a slender column in the corner  $t_\epsilon$ , negligible inertia  $t_{visc}$  and a slender column throughout the container  $t_{\epsilon R}$  are shown.

meniscus approaches zero. For these tests, repeat measurements of a single test event show measurement repeatability of  $\pm 3$ –6% when comparing fit coefficients.

#### 4.4. Surface profile, $h(z, t)$

Four tests of the capillary rise of PDMS in equilateral triangular cells ( $\alpha = 30^\circ$ ) are chosen for detailed measurement. These tests are representative of the parametric range of  $Su$  accessed in the drop tower experiments, see table 6. The four runs are selected from a family of tests conducted to explore repeatability and sensitivity to container surface conditions. Within each family, the measurements of the surface profiles are statistically equivalent whether the containers are initially dry or are pre-wetted with a thin film of the test fluid, whether minutes or days, prior to the test. This agreement is not common for spontaneous capillary flows (Mumley, Radke & Williams 1986; Weislogel 1997), but may occur for these tests because of the natural pre-wetting of the corner.

Ten digitized surface traces for the corner flow of test LT2 are presented in figure 12. These data are acquired using an automated image analysis system which digitizes the cinefilm records for selected frames and tracks the development of the meniscus in time. The grabbed images are low-pass filtered and a median threshold is selected to define the interface which is then skeletonized. Figure 12(a) suggests that there is a location  $z = z_H \simeq 11$  mm such that the height  $h(z_H, t) \equiv H$  is fixed for sufficiently long times  $t > t_H$ . A magnification of the region near this location shows that all of the curves for  $t > t_H \simeq 0.4$ s pass through a narrow neighbourhood near  $z_H$ , figure 12(b). Measurements of the local centreline height,  $h(z_i, t)$ , at several  $z$ -locations,  $z_i$ , in this region are presented in figure 13, where the distance between each  $z_i$  is approximately 1.5 mm. As can be seen from the figure, depending on  $z_i$ ,  $h(z_i, t)$  will in general under- or overshoot  $h(z_H, t) \equiv H$ . The curves for  $t > 0.7$  s are fit with linear coefficients to locate  $z = z_H$  such that  $h(z_H, t) = H_{exp} = \text{const}$ . Interpolation between the smallest positive and negative slopes provides the empirically determined  $z = z_H = 11.24$  mm and  $H_{exp} = 3.73 \pm 0.15$  mm. This location then defines the apparent origin where the constant height boundary condition of the asymptotic analysis can be applied. In subsequent figures, the origin is moved to  $z = z_H$ . Downstream of this location  $h$  is always increasing towards  $H$  while upstream  $h$  is decreasing everywhere to this same level. Since only limited time was available for these tests the long-time behaviour of the boundary condition at  $z_H$  cannot truly be confirmed. However, the results of Dong & Chatzis whose experiments lasted hours offer strong evidence that the constant height ('constant pressure') condition is acceptable. The value  $H_{3-poly} = 3.67$  mm

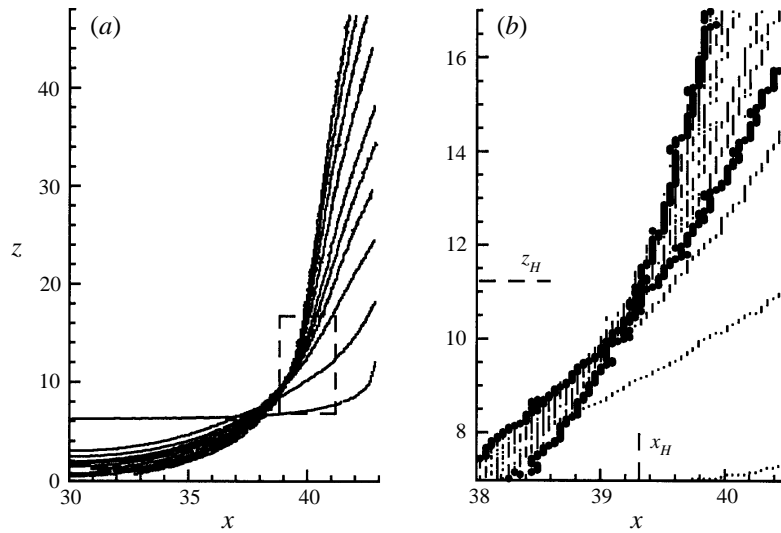


FIGURE 12. The interface height  $h(z,t)$  measured along the  $x$ -axis for LT2. (See table 6 for the parameters of this run.) The coordinates  $x$  and  $z$  are in mm, with an arbitrary origin. The centreline of the cell is located at  $x \approx 30$  mm and the corner is at  $x = 43.0$  mm. Before the rig is dropped, except for the meniscus near the corner, the interface is located along  $z_0$ . During free fall, as time increases the profiles advance along the corner and recede at the centreline. The surface profiles are shown for times  $t = 0, 0.078, 0.156, 0.234, 0.312, 0.390, 0.547, 0.703, 0.859,$  and  $1.015$  s. (a) Global profiles from the wall to cell centreline. (b) Enlarged view of dashed box area on (a). Coordinates of the constant height location  $(x_H, z_H)$  are indicated. Except for the three earliest times, all profiles pass close by  $(x_H, z_H)$ .

determined analytically from (3.5), compares well with the experimental value for this test. The values of  $H_{exp}$  for all four runs show good agreement with  $H_{3-poly}$ , see table 6.

The experimental values for  $t_H$  are included in table 6. These values, along with  $z_H$  for each test, are used as the space and time origins in figures 14 and 15 which show the scaled 'height'  $F^+$  as a function of the scaled 'distance'  $\eta^+$  ( $a = 0$ ) for the four tests. The similarity solution presented in §3.1 is provided for comparison.

Figures 14 and 15 reveal that, in general, the measured height is converging to the analytical result as time increases. However, these figures also show a progressively poorer description of the flow with increasing viscosity and cell size. Agreement between experiment and theory is especially good in figure 14 in a lengthening region from  $\eta^+ = 0$  downstream. The most persistent discrepancy between theory and measurement is near the tip, yet nearly full agreement is achieved by the end of the tests. The lack of such agreement in figure 15 will be addressed in the next section.

## 5. Discussion: capillary rise

For the capillary rise problem, as the fluid column extends in length along the corner, the time for information about the upstream boundary condition to propagate downstream to the tip is  $\sim \mathcal{L}^2$ . Consequently, though the constant height boundary condition is established at  $t = t_H$ , the region near the tip will not respond to this condition until some time later. Thus, for a time, the tip region acts independently of changes in conditions at the origin. In order to determine the scaling suitable to the tip region, the surface profile measurements were analysed for  $t < t_H$ . As an example,

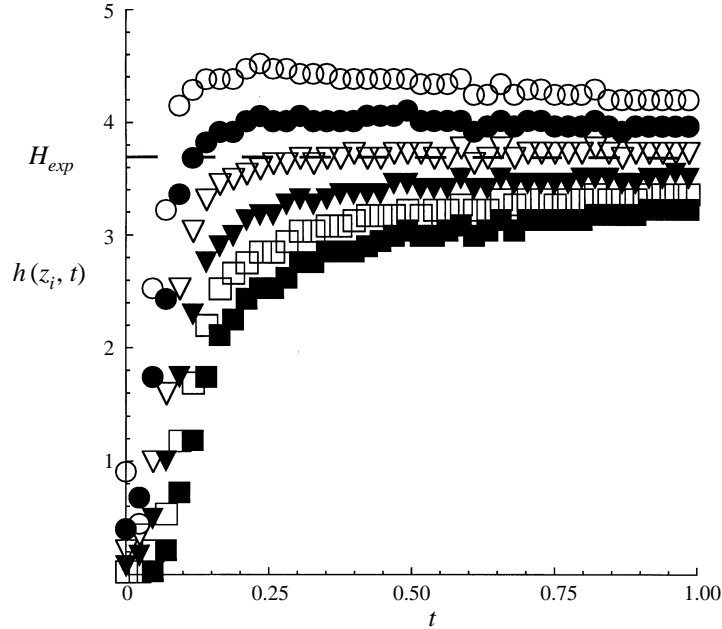


FIGURE 13.  $h(z_i, t)$  (mm) as a function of  $t$  (s) for LT2, the run shown in figure 12. Each of the six data sets is taken for constant  $z_i$  with an increment of approximately 1.5 mm between each  $z_i$ . With linear fits to the data for  $t > 0.7$  s, interpolation yields the  $z$ -location for which the variation of  $h$  with time is zero:  $z_H = 11.24$  mm, where  $H_{exp} = 3.73 \pm 0.15$  mm and is shown by the dashed line. This value compares favourably with  $H_{3-poly} = 3.67$  mm as determined from (3.5).

figure 16 displays  $h(z_H, t)$  for test ST10.  $H_{exp}$  and  $t_H$  are provided on the figure for reference.

It is seen that the slope  $a \approx 1/5$  models a significant duration of the ‘start-up’ flow prior to the establishment of the constant height condition, though preliminary tests indicate that this behaviour may not be universal. The data at the earliest times may be captured by the length-scale-independent linear solution with  $a = 1$ , but not enough data are available to be conclusive. As shown in §3.2, the case  $a = 1/5$  models a constant inlet flow rate. By choosing the tip of the flow as the origin, the data of figure 14(b) are rescaled by using  $a = 1/5$  and plotted in figure 17. A general collapse of the data for  $t < t_H$  is established over the entire interval  $0 \leq \eta^+ \leq 1$ , shown by the small dots. For  $t \gtrsim t_H$  the solution becomes an increasingly poorer description of the flow near  $\eta^+ = 0$  as shown by the larger symbols (same symbols as used in figure 14(b)). Also, note from figure 17 that for all times the surface traces generally collapse near the tip. This feature illustrates the insensitivity of the flow/solution near the tip to the value of the similarity parameter  $a$ .

### 5.1. Start-up

The release mechanism used in the drop tower experiments provides a nearly discontinuous reduction of  $g$  by severing a wire supporting the experiment. The initial response of the fluid to this sudden reduction in body force is complicated by inertia. If the Bond number ( $Bo_i \equiv \rho g R^2 / \sigma$ ) of the system prior to release is large, the fluid experiences a number of inertial regimes.

When  $Bo_i \gg 1$  the only interfacial length scale is the capillary length  $L_c \sim (\sigma / \rho g)^{1/2}$ . This length is independent of any system (container) length scale,  $R$ , provided

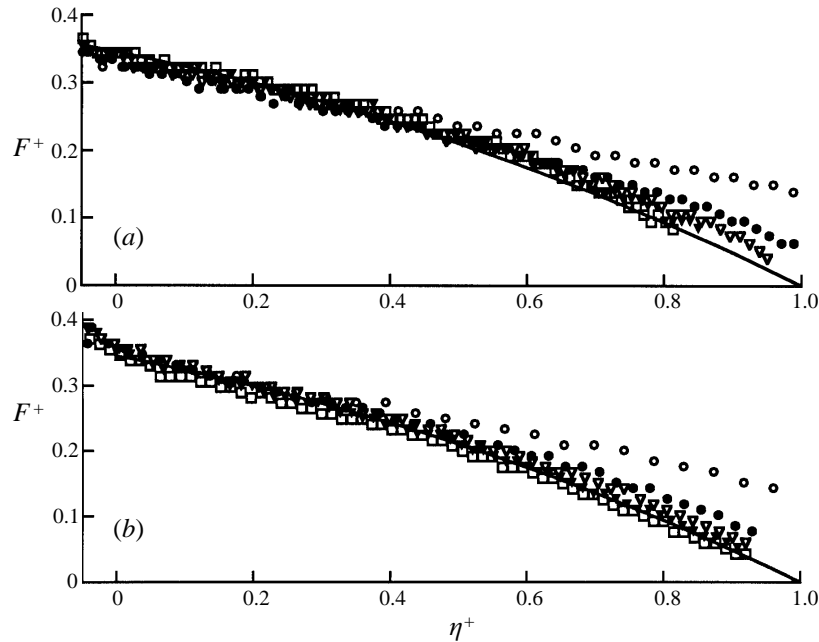


FIGURE 14. The evolution of the interface in terms of the similarity variables  $F^+(\eta^+)$  for the smaller container,  $D = 12.0$  mm. The solution from (3.2) for  $a = 0$  is shown as the solid line. The measurements are shown as symbols. The largest difference between measurement and theory, near the tip  $\eta^+ = 1$ , diminishes with increasing time. (a) Test ST1:  $\nu = 1$  cS at times  $\circ$ , 0.352;  $\bullet$ , 0.508;  $\nabla$ , 0.664;  $\nabla$ , 0.820 and  $\square$ , 0.977. (b) Test ST10:  $\nu = 10$  cS, at times  $\circ$  0.586,  $\bullet$ , 0.976;  $\nabla$  1.367,  $\nabla$ , 1.758 and  $\square$ , 2.031. All times are in (s).

$L_c/R \ll 1$ . It can be shown that the initial inertial response of the interface occurs within

$$t_{L_c} \sim (\rho L_c^3 / \sigma)^{1/2} \sim (\sigma / \rho g^3)^{1/4}. \quad (5.1)$$

Such inertial transients have been studied previously regarding the response of an interface in a circular cylinder to a step reduction in gravity level (Siegert, Petrash & Otto 1964; Weislogel & Ross 1990 and Wolk *et al.* 1997). As an example, Siegert *et al.* (1964) find that  $t_{L_c} = C(\rho R^3 / \sigma)^{1/2}$ , where  $R$  is a characteristic length and  $C$  is a constant which depends on the container geometry; for a right circular cylinder of radius  $R$ ,  $C = 0.413$ . For these tests, if  $R$  is taken as the distance of the container axis to the meniscus centreline at  $z_H$ , for the equilateral triangle,  $R = D/\sqrt{3} - H$ , and thus, using  $C = 0.413$ ,  $t_{L_c}$  is determined to be 0.080 s for LT2 and 0.031 s for ST10. These values are comparable to the 'reorientation time' of the bulk menisci extrapolated from measurement, figure 18, where it is seen that  $t_{L_c} \approx 0.09$  s for LT2 and  $\approx 0.03$  s for ST10. Part of this initial response is the production of capillary waves of wave-length  $L_c$  which emanate from the contact line region and propagate with velocity  $U_{L_c} \sim (\sigma g / \rho)^{1/4}$  across the surface. So the container length scale becomes relevant after a characteristic time

$$t_{RL_c} \sim R / U_{L_c} \sim R (\rho / \sigma g)^{1/4}. \quad (5.2)$$

The inertial response of the entire system then dominates and is characterized by

$$t_R \sim (\rho R^3 / \sigma)^{1/2}. \quad (5.3)$$

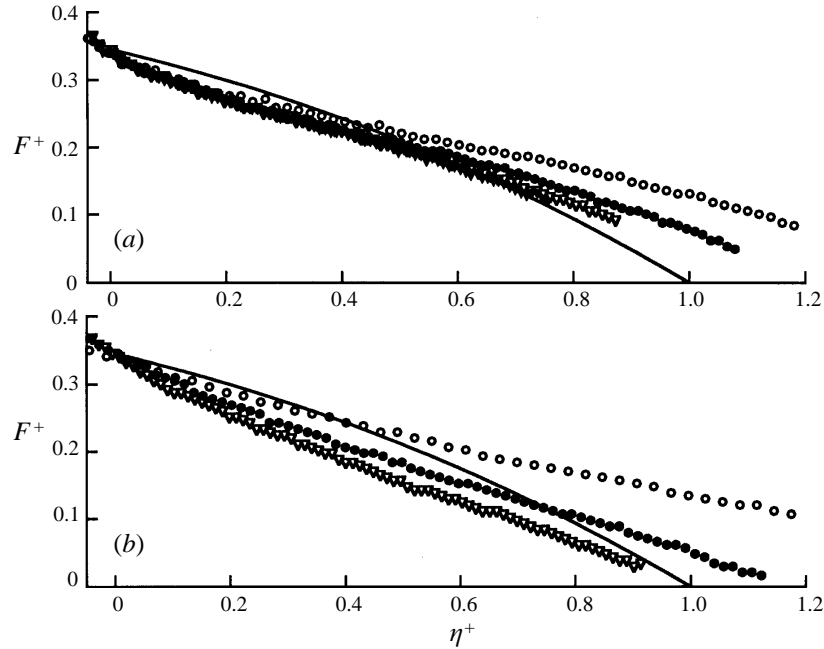


FIGURE 15. As figure 14 but for the larger container,  $D = 22.6$  mm. The agreement with theory is not as good as for the smaller container shown in figure 14. (a) Test LT2:  $\nu = 2$  cS, at times  $\circ$ , 0.547;  $\bullet$ , 0.703;  $\nabla$ , 0.859 and  $\nabla$ , 0.977. (b) Test LT20:  $\nu = 20$  cS at times  $\circ$ , 1.17;  $\bullet$ , 1.56 and  $\nabla$ , 2.07. All times are in (s).

If  $Bo_i \lesssim O(1)$  prior to release,  $L_c \approx R$  and the manifold inertial time regimes described by (5.1)–(5.3) above reduce to the single time scale given by (5.3), since in this limit  $t_{L_c} = t_{RL_c} = t_R$ .

The scenario that emerges, then, is as follows. Initially the flow is inertially dominated. A linear transient  $a = 1$  may then follow. Afterwards, the fluid is drawn into the corner according to the  $a \approx 1/5$  solution. As the fluid redistributes, after some time  $t_H$ , a constant height boundary condition is established where the  $a = 0$  similarity solution is applicable. In the overlap period between  $a = 1/5$  and  $a = 0$  behaviour, the constant height boundary condition imposes itself on a lengthening interval, chasing the  $a = 1/5$  tip solution and finally overwhelming it. What will be observed, then, is a flow which, at first, grows linearly with time  $\sim t$ , followed by  $\sim t^{3/5}$  growth leading into the  $\sim t^{1/2}$  growth characteristic of the constant-height boundary condition. A sequence of transitions between flow regimes is also seen by Dreyer, Delgado & Rath (1994) for the transient capillary rise of a liquid index between parallel plates where the column height progresses from inertial ( $\sim t^2$ ), to entrance region ( $\sim t$ ), to viscous ( $\sim t^{1/2}$ ) regimes.

## 5.2. Time scales for validation of theory, discussion

The time scales required for validation of the slender column and negligible inertia assumptions for the corner flow solutions can be computed using the solution for  $\mathcal{L}(t)$  with  $\epsilon = H/\mathcal{L}(t)$ ,

$$\epsilon^2 \ll 1 \quad \text{yields} \quad t \gg t_\epsilon \equiv 0.345\mu H f / \sigma F_i \sin^2 \alpha, \quad (5.4)$$

$$\mathcal{R} \ll 1 \quad \text{yields} \quad t \gg t_{\text{visc}} \equiv 0.5H^2 \sin^2 \alpha / F_i \nu, \quad (5.5)$$

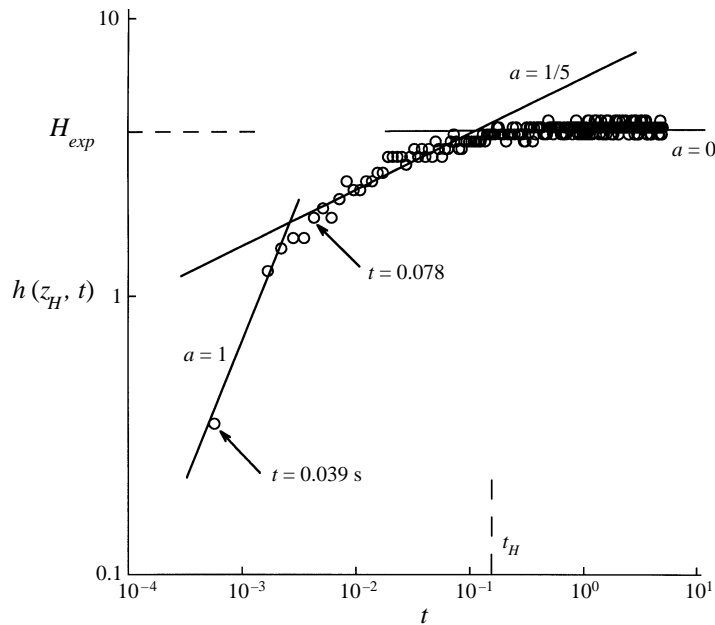


FIGURE 16. The interface height  $h(z_H, t)$  for ST10 measured at the axial location where the constant height  $H$  is established for  $t > t_H$ . Prior to  $t_H$ , beginning at about  $t = 0.078$  s, the height increases with a slope  $a = 1/5$  indicating that the constant flow rate similarity solution of §3.2 models the flow. Though the data are too sparse to show it definitively, the length-scale-independent solution which yields linear growth,  $a = 1$ , may model the flow at early times. The first data point is at time  $t = 0.039$  s.

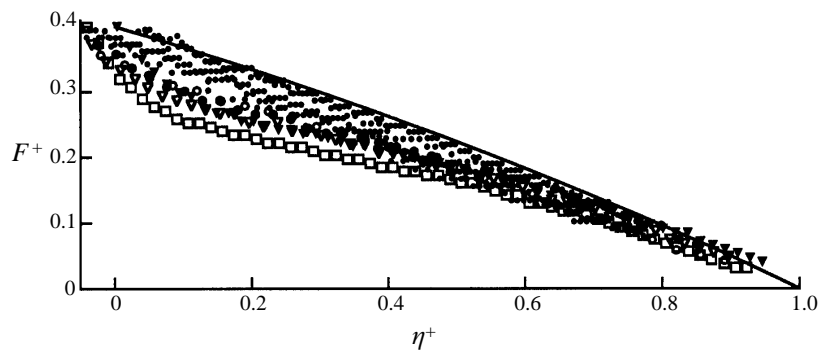


FIGURE 17. Interface height for test ST10 in which the data have been measured from a common tip location  $\eta^+ = 1$ . For times  $t < t_H$ , small solid dots, the measurement and the constant flow rate similarity solution ( $a = 1/5$ ) of §3.2 agree. The times  $t > t_H$  are shown by the same larger symbols as in figure 14(b); as time increases the constant flow rate solution becomes an increasingly poor description, as the  $a = 0$  solution (of figure 14b) becomes established over an increasing interval in  $\eta^+$ . Note that the slope at the tip, which is independent of  $a$ , matches the similarity solution for all time.

respectively. Times  $t_\epsilon$  and  $t_{visc}$  are computed and listed in table 6. For the tests under consideration,  $f = 1$ . Thus, the slender column and slight corner axis curvature requirements are equivalent.

The above scales are in general satisfied for the test data presented. However, for the time available during the drop tests, a general decrease in agreement is observed

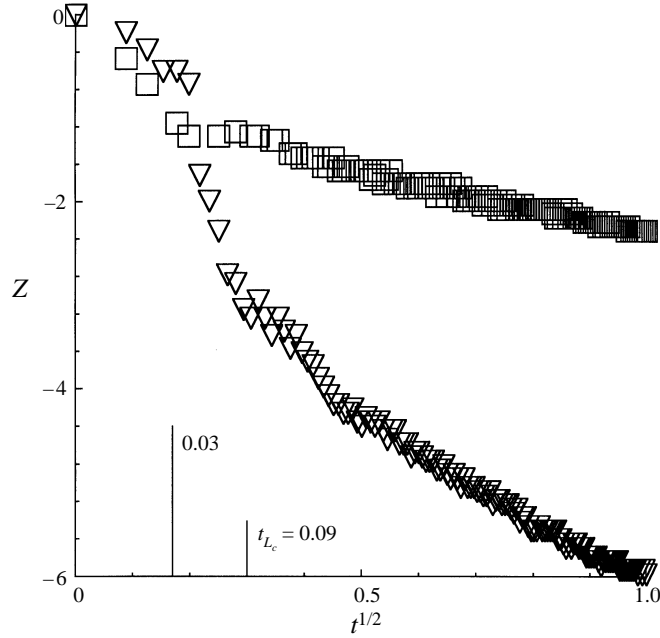


FIGURE 18. The axial location  $Z$  (mm) of the receding bulk meniscus as a function of  $t$  (s) for tests ST10 ( $\square$ ) and LT2 ( $\nabla$ ). The distance  $Z$  is measured from the lowest point of the bulk meniscus (see figure 2). The inertial time  $t_{Lc}$  indicates the transition from inertial reorientation to the capillary flow regime,  $t_{Lc} = 0.03$  (0.09) for  $\square$  ( $\nabla$ ).

with increasing viscosity (cell size fixed) and increasing cell size (viscosity fixed). This disagreement is most noticeable in the curvature along the flow direction, see figure 15(b), in which upstream of an inflection point, the curvature of the data is opposite to that of the theory. As time increases, more fluid is pumped into the corner and the inflection point moves upstream until it is eventually out of the similarity solution regime described by  $\eta^+ > 0$ . The discrepant corner axis curvature may be interpreted as the influence of bulk meniscus curvature, see §6. This influence wanes with time as the bulk meniscus recedes upstream, farther from the location of the constant height condition.

The fact that the disagreement increases with increasing viscosity argues against the influence of the viscous time scale  $t_{visc}$  based on  $\mathcal{R} \ll 1$ . This is surprising on the grounds that the viscous time scale  $R^2/\nu$  based on container size is often large (e.g.  $\sim O(5)$  s) for ST1 and  $\sim O(10)$  s) for LT2, and up to  $\sim O(40)$  s) for some of the tests performed)! The slender column assumptions  $\epsilon^2 \ll 1$  and  $\epsilon^2 f \ll 1$  capture the correct trends, namely  $t \sim \mu H/\sigma$ , but have short time scales. While the original scaling of the problem was based on the isolated flow in the corner where the height of fluid is characterized by  $H$ , when addressing the global container flow,  $R$  should replace  $H$ . Typical values for this global time scale  $t_{\epsilon_R}$ , which characterizes the time for the flow throughout the container to be slender  $\epsilon_R^2 \equiv (R/\mathcal{L}(t))^2 \ll 1$  are listed in table 6. Test ST1 (figure 14a) is well described by the theory by the end of the run at  $1 > t_{\epsilon_R} = 0.17$  s while test LT20 (figure 15b) is not fully described by the theory by the end of its run at  $2 \not> t_{\epsilon_R} = 6.5$  s. This suggests that container-sized curvature may set the time scale at which the theory becomes applicable.

Consider, as described earlier for systems with  $Bo_i \gg 1$  at time  $t = 0^-$ , that



the initial inertial response of the fluid is governed by the length scale  $L_c$  which is independent of container size. Thus, the flow rate for the start-up problem should be independent of container size. If this is true, a larger amount of fluid per container cross-sectional area rises in a smaller container than in a larger container during  $0 < t < t_H$ . This implies that, for fixed fluid properties, the bulk meniscus is further upstream from the constant height location in smaller containers at  $t_H$ . We speculate that the influence of the bulk meniscus curvature may be significantly stronger in a larger container due to its proximity to the constant height location at  $t_H$ .

**6. Global similarity solution: capillary rise**

A ‘global’ similarity solution may be developed for the capillary rise problem exploiting insights from the experimental observations, §4 and §5. The solution is appropriate for large times and is applicable throughout the container, not just downstream of the constant height location.

Dong & Chatzis (1995) conducted experiments for long times  $t/t_H \gg 1$  and found that the centreline of the bulk meniscus recedes upstream  $\sim t^{1/2}$ . So for long times, this point can be described by  $\eta^+ \equiv \eta_b^+ = \text{const} < 0$ . In the region of the bulk meniscus, axial curvature is comparable to transverse curvature so the asymptotic analysis cannot be applied. Postulating that this region is of fixed length or, at most, grows like  $t^\gamma$  where  $\gamma < 1/2$ , the bulk meniscus region shrinks to a single location  $\eta_b^+$  as  $t \rightarrow \infty$  and for long times the asymptotic analysis can be applied throughout the flow domain. Application of these observations leads to a similarity solution  $F^+(\eta^+)$  valid over the entire flow domain  $\eta_b^+ \leq \eta^+ \leq 1$ .

To determine a global solution, (3.2) is augmented by the integral mass balance, which, after substituting  $\lambda^2 = 1/F^+(0)$  and  $H \equiv F_H D$ , becomes

$$-A_1 \eta_b^+ F_H^{-2} F^{+2}(0) = \int_{\eta_b^+}^1 F^{+2} d\eta^+, \tag{6.1}$$

where, for the  $n$ -polygon, the scaled sector area is given by  $A_1 = (1/4F_A) \cot \pi/n$ . As discussed in §3.1,  $F_H$  may be approximated using the technique of de Lazzer *et al.* (1996). Equation (6.1) may then be solved directly for  $\eta_b^+$ ; for run ST1 this yields the vertical segment  $\eta_b^+ = -0.058 \dots$  which serves as a limit to the data as  $t \rightarrow \infty$ , figure 19.

Since the upstream moving bulk meniscus appears to approach an invariant shape for long times, the pressure in the cap also approaches a constant. Thus, rather than apply the constant pressure condition at the origin, it can be applied at  $\eta_b^+$ . It now is appropriate to non-dimensionalize the formulation based on the height  $H_b$ , which characterizes the bulk meniscus region, rather than on  $H$ . The invariant form of governing equation (3.2) remains unchanged, but is now subject to  $h = 1 = F(\eta_b)$  and the integral mass balance

$$-A_1 \eta_b^+ F_b^{-2} F^{+2}(\eta_b^+) = \int_{\eta_b^+}^1 F^{+2} d\eta^+, \tag{6.2}$$

where  $\lambda^2 = 1/F^+(\eta_b^+)$  and  $H_b \equiv F_b D$ . After  $F^+$  is determined by solving the invariant governing equation, (6.2) may be solved directly for  $\eta_b^+$  allowing  $\lambda$  and hence  $\eta_{tip}$  to be determined. This solution formulation produces the constant height location at  $\eta = 0$  as a byproduct. In order to implement this method of solution, the pressure in the cap or, equivalently,  $H_b$  needs to be evaluated. However, we are unaware of

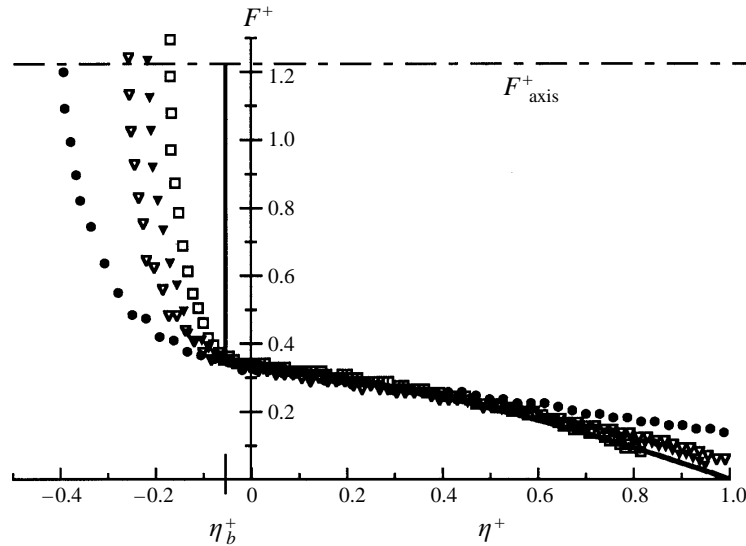


FIGURE 19. The region in which three-dimensional effects are important shrinks to a point  $\eta^+ = \eta_b^+$  as  $t \rightarrow \infty$ . So, for long times, the constant height similarity solution ( $a = 0$ ), shown by the solid line, can be extended upstream of the origin,  $\eta^+ < 0$ . As time increases, the data from test ST1 (using the same symbols as in figure 14a) approach the long-time solution throughout the domain. In particular, note that the data from the bulk meniscus region tend to the vertical line at  $\eta^+ = \eta_b^+$ .

any solution to the three-dimensional geometry for  $t \rightarrow \infty$  which would yield these values. It is interesting to note, though, that for a broad range of upstream conditions  $F_H \leq F_b \leq 2F_H$  the tip location varies only slightly  $1.605 \leq \eta_{tip} \leq 1.702$ . This further testifies to the tip solution being insensitive to the upstream boundary conditions.

## 7. Summary of results

In this work the equations describing capillary flows in containers with interior corners are analysed under the constraints of a slender fluid column, slight surface curvature along the flow direction, low inertia, and low gravity. The quasi-steady viscous streamwise flow is solved, averaged over the cross-sectional area, and using a local mass balance a second-order nonlinear diffusion equation for the height of the meniscus  $h(z, t)$  is derived.

Attention is given to the scaling. The velocity scale accounts explicitly for much of the variation of the flow resistance coefficient; the contribution which must be evaluated numerically varies only slightly,  $1/8 \lesssim F_i \leq 1/6$ . The scaling also clarifies the geometric influence of corner half-angle  $\alpha$  and contact angle  $\theta$  to permit the effects of container size, container geometry (including aspect ratio), and system contact angle, whether static or dynamic, to be assessed by inspection of the closed form results, see table 3 and §3.4.

A generalized similarity equation is solved for a range of the transform parameter,  $a$ , and it is shown that a linear tip solution is valid near the tip for any choice of  $a$ . The similarity solution of Dong & Chatzis (1995) for the case of a capillary flow in an initially empty corner, where at time  $t = 0^+$  fluid is introduced at a constant height of the meniscus  $h(0, t) = H$ , is re-formulated and solved ( $a = 0$ ). This is called the ‘capillary rise’ problem in this study. Similarity solutions for a constant inlet

flow condition, a spreading drop (constant volume), and an exponential inlet flow condition are also listed. It can be shown that the constant flow and constant volume problems yield minimized time constants for  $\alpha \simeq 17^\circ$ ,  $\theta = 0$ , while the constant height and exponential flows are minimized when  $\alpha \simeq 30^\circ$ ,  $\theta = 0$ .

Test data are presented for the specific problem of capillary rise in interior corners after a step reduction in gravity. An extensive data set over a previously unexplored range of flow parameters is collected using a 2.2 s drop tower. Measurements using a zero contact angle fluid ( $\theta = 0$ ) reveal repeatability and accuracy, the role of inertia and column slenderness, and the effects of corner half-angle, container size, container aspect ratio, and fluid properties.

The initial transient due to the step reduction of gravity, characteristic of most drop tower tests, is governed by the inertial response time of the interface,  $t_{L_c}$ . The flow at small times may be length-scale independent as modelled by the similarity solution with  $a = 1$ . An experimental data set is presented which demonstrates that for intermediate times the flow is described by a constant flow-like similarity solution, where  $a \approx 1/5$ . Preliminary results on other runs indicate that the value of  $a$  which best models the flow for these intermediate times may not be universal.

A location along the interface which remains stationary as the flow evolves was found. This value agrees favourably with that computed using the method of de Lazzar *et al.* (1996) for static interfaces. This constant height condition yields a similarity solution with  $t^{1/2}$  dependence for the flow. The time  $t_H$  required to establish this constant height is used as the time origin for comparisons of the similarity solution to the experimental results. The experiments agree well with the analysis in an expanding interval extending downstream from the constant height location. As flow along the corner begins prior to  $t_H$ , the tip location is not well predicted at short times.

Measurements made in smaller containers compare better with theory. This agreement is not due to the diminished role of inertia or a more dominant presence of viscous effects. The time scales on which viscous forces come into play are comparable to the total time of the experiments (see table 6). Furthermore, it is found that agreement between theory and experiment improves as viscosity decreases. It appears, then, that the rapid establishment of parallel flow alone validates the asymptotic analysis. We speculate that the improved agreement with decreasing container size is attributable to the diminished role of three-dimensional interface curvature arising from the bulk meniscus.

A global similarity solution for the capillary rise problem was formulated which describes the flow throughout the container at long times. The domain of the similarity solution is then set by an integral mass balance equation. The boundary conditions for the problem include the specification of the pressure in the liquid at a location where  $\eta^+ = \text{const}$ .

In overview, then, it is observed that the initial transient experienced by the fluid is governed first by inertia during the formation of the capillary surface  $t \lesssim t_o$  (where perhaps  $\mathcal{L} \sim t$  as given by a linear solution), then by a constant flow-like regime for  $t_o \lesssim t \lesssim t_H$  ( $\mathcal{L} \sim t^{3/5}$ ), then by an overlap regime beginning at  $t \simeq t_H$  in which the constant height similarity profile extending from the origin is joined to a tip solution, and finally by the constant height solution alone for  $t \gg t_H$  ( $\mathcal{L} \sim t^{1/2}$ ).

Direct application of the results contained herein may be made to fluid systems in the low-gravity environment of space. Because the flow is to a large extent controlled by the nearly parallel flow along the corner, inertia may be successfully ignored. The large length scale systems which can arise in the low-g environment produce fast flows

(large  $Su$ ) several orders of magnitude larger than in similar terrestrial flows. Low- $g$  experiments with spreading drops in open corners may provide an excellent data base with which to compare further analyses: for this flow scenario an exact analytical expression is available, and the influence of first-order inertia, dynamic contact angle, and/or corner-axis curvature may then be incorporated within an asymptotic analysis.

Support for this work was provided by NASA's Microgravity Science and Application Division, NASA Lewis Research Center, and the Office of Naval Research under grant N00014-92-1-1137. M.M.W. acknowledges his good fortune of having as colleagues R. Balasubramaniam, Paul Concus, Robert Finn, and Dieter Langbein. Lloyd Trefethen and Andrew J. Bernoff are thanked for helpful discussion. Jennifer Kadlowec, Mike Luli, and Mark Pillar provided assistance in the collection of the data.

### Appendix. $F_i$ solution detail

In this Appendix two approximate expressions,  $F_I$  and  $F_{II}$ , are found for the flow resistance coefficient  $F_i$  in the limit of small and large corner half-angle  $\alpha$ , respectively. An exact solution  $F_{III}$  is also presented. These solutions are shown on figure 6.

#### $F_I$ , Small corner angle solution, $\tan^2 \alpha \ll 1$

In the limit  $\alpha^2 \ll 1$ , an expansion for  $w_o$  may be written  $w_o = w_{o_0} + w_{o_1} \tan^2 \alpha + \dots$  and when substituted into (2.5) yields  $w_o = P_{oz}(y^2 - x^2)/2 \cos 2\alpha$ . The average velocity,  $\langle w_o \rangle_I$ , may in turn be determined using

$$\langle w_o \rangle_I = -\frac{P_{oz} \tan \alpha}{h^2 F_A \cos 2\alpha} \int_0^{y_m} \int_y^{S_o} (y^2 - x^2) dx dy. \quad (\text{A } 1)$$

Upon substitution of the quantities  $P_o$ ,  $S_o$ ,  $y_m$ , and  $f$  from (2.7)–(2.10), the above integration yields  $\langle w_o \rangle_I = -F_I h_z$ . Some limiting values of  $F_I$  are

$$F_I(\delta^2 \ll 1) = 1/6 + \alpha^2/3 + \alpha\delta/90 + O(\alpha^4, \delta\alpha^3, \delta^2\alpha^2, \delta^3\alpha, \delta^4),$$

$$F_I(\delta = \pi/2 - \alpha) = \frac{1}{6} + \frac{\alpha}{3} \left(1 - \frac{5\pi}{16}\right) + \frac{\alpha^2}{2} \left(3 - \frac{5\pi}{12} - \frac{5\pi^2}{48}\right) + O(\alpha^3),$$

which reveal that in the limit  $\tan^2 \alpha \rightarrow 0$ ,  $F_I \rightarrow 1/6$ , and thus  $\langle w_o \rangle = -h_z/6$ .

#### $F_{II}$ , large corner angle solution, $\Omega^2 \ll 1$

Substituting  $\Omega (\equiv \pi/2 - \alpha)$  for  $\alpha$  and dividing by  $\sin^2 \alpha$  (2.5) in the limit  $\Omega^2 \ll 1$  becomes  $\bar{P}_{oz} = w_{o_{xx}} + \Omega^2 w_{o_{yy}}$ , subject to  $w_o = 0$  on  $x = y$  and  $w_{o_x} - \Omega^2 S_{o_y} w_{o_y} = 0$  on  $x = S_o$ , where  $\bar{P}_o = P_o / \cos^2 \Omega$ . The system for  $w_o = w_{o_0} + \Omega^2 w_{o_1} + \dots$  is solved yielding

$$w_{o_0} = \bar{P}_{oz} (x^2/2 - y^2/2 + h(y - x)), \quad (\text{A } 2)$$

$$w_{o_1} = w_{o_0} + \bar{P}_{oz} \left[ \frac{yk}{h} (2y^2 - x^2 - xy) + \frac{k}{6h} (x^3 - 3x^2y + 2y^3) \right. \\ \left. + \left( 4yk + \frac{y^2k^2}{h^2} \left( y - \frac{3h}{2} \right) - \frac{kh}{2} \right) (x - y) \right], \quad (\text{A } 3)$$

where  $k = \phi(1 - \phi/2)$  and  $\phi \equiv \delta/\Omega$ . Note that these expansions are correct regardless of the sign of  $\delta$  as long as  $\delta^2 \ll 1$  is maintained. In this way positively and negatively

curved surfaces may be solved. No solution of this nature is possible for  $|\delta| \sim O(1)$ . The average velocity  $\langle w_o \rangle_{II}$  is determined to  $O(\Omega^2)$  using

$$\langle w_o \rangle_{II} = \frac{2 \cot \Omega}{h^2 F_A} \int_0^{y_m} \int_y^{S_o} (w_{o_o} + \Omega^2 w_{o_1}) dx dy. \quad (A 4)$$

Performing the integration produces  $\langle w_o \rangle_{II} = -F_{II} h_z$ . Some limiting values of  $F_{II}$  are

$$F_{II}(\phi = 0) = 1/6 + \Omega^2/3 + O(\Omega^4),$$

$$F_{II}(\phi = 1) = 1/7 + 49\Omega^2/180 + O(\Omega^4),$$

$$F_{II}(\phi = -1) = 0.183 + 0.391\Omega^2 + O(\Omega^4).$$

$$F_{III}, \text{ Exact solution, } \alpha = \theta = \pi/4$$

An analytic solution for  $F_i$  is adapted from classic solutions of viscous flows in non-circular ducts (White 1974). For the case  $\alpha = \pi/4$ ,  $\theta = \pi/4$ ,  $\delta = 0$ , it can be shown that

$$F_{III} = -\frac{1}{3} \left[ 1 - \frac{192}{\pi^5} \sum_{i=1,3,5,\dots}^{\infty} \frac{\tanh i\pi/2}{i^5} \right] = 0.14057 \dots \quad (A 5)$$

#### REFERENCES

- AYYASWAMY, P. S., CATTON, I. & EDWARDS, D. K. 1974 Capillary flow in triangular grooves. *Trans. ASME: J. Appl. Mech.* **41**, 332–336.
- BARENBLATT, G. I. & ZEL'DOVICH, YA. B. 1972 Self-similar solutions as intermediate asymptotics. *Ann. Rev. Fluid Mech.* **4**, 285–312.
- CONCUS, P. & FINN, R. 1969 On the behavior of a capillary surface in a wedge. *Appl. Math. Sci.* **63**, 292–299.
- CONCUS, P. & FINN, R. 1974a On capillary free surfaces in the absence of gravity. *Acta Math.* **132**, 177–198.
- CONCUS, P. & FINN, R. 1974b On capillary free surfaces in a gravitational field. *Acta Math.* **132**, 207–223.
- CONCUS, P. & FINN, R. 1990 Capillary surfaces in microgravity. In *Low-Gravity Fluid Dynamics and Transport Phenomena*. (ed. J. N. Koster & R. L. Sani). Progress in Astronautics and Aeronautics, Vol. 130, pp. 183–204. AIAA.
- DONG, M. & CHATZIS, I. 1995 The imbibition and flow of a wetting liquid along the corners of a square capillary tube. *J. Colloid Interface Sci.* **172**, 278–288.
- DREYER, M., DELGADO, A. & RATH, H. J. 1994 Capillary rise of a liquid between parallel plates under microgravity. *J. Colloid Interface Sci.* **163**, 158–168.
- DUSSAN V., E. B. 1979 On the spreading of liquids on solid surface static and dynamic contact lines. *Ann. Rev. Fluid Mech.* **11**, 371–400.
- JAEKLE, D. E. JR 1991 Propellant management device conceptual design and analysis: vanes. *AIAA Paper* 91-2172.
- KISTLER, S. F. 1993 Hydrodynamics of wetting. In *Wettability*. Surfactant Science Series, (ed. Berg, J. C.). vol. **49**, Chapter 6, 311–429.
- KOLB, W. B. & CERRO, R. L. 1993 The motion of long bubbles in tubes of square cross section. *Phys. Fluids A* **5**, 1549–1557.
- KOSTER, J. N. & SANI, R. L. 1990 *Low-Gravity Fluid Dynamics and Transport Phenomena*. Progress in Astronautics and Aeronautics, vol. 130, AIAA.
- KOVSCHEK, A. R. & RADKE, C. J. 1996 Gas bubble snap-off under pressure driven flow in constricted noncircular capillaries. *Colloids and Surfaces A* **117**, 56–76.
- LANGBEIN, D. 1990 The shape and stability of liquid menisci at solid edges. *J. Fluid Mech.* **213**, 251–265.

- LAZZER, A. DE, LANGBEIN, D., DREYER, M. & RATH, J. 1996 Mean curvature of liquid surfaces in containers of arbitrary cross-section, *Microgravity Sci. Technol.* **IX**(3), 208–219.
- LEGAIT, B. 1983 Laminar flow of two phases through a capillary tube with variable square cross-section. *J. Colloid Interface Sci.* **96**, 28–38.
- LEKAN, J., GOTTI, D., JENKINS, A. J., OWENS, J. C. & JOHNSTON, M. R. 1996 Users guide for the 2.2 second drop tower of the NASA Lewis Research Center. *NASA TM 107090*.
- LENORMAND, R. & ZARCONI, C. 1984 Role of roughness and edges during imbibition in square capillaries. SPE 13264, presented at the 59th Annual Meeting of the SPE, Houston, TX.
- MA, H. B., PETERSON, G. P. & LU, X. 1994 The influence of vapor-liquid interactions on the liquid pressure drop in triangular microgrooves. *Intl J. Heat Mass Transfer* **37**, 2211–2219.
- MARSHAK, R. E. 1958 Effect of radiation on shock wave behavior. *Phys. Fluids* **1**, 24–29.
- MASON, G. & MORROW, N. 1991 Capillary behavior of a perfectly wetting liquid in irregular triangular tubes. *J. Colloid Interface Sci.* **141**, 262–274.
- MAYER, F. J., MCGRATH, J. F. & STEELE, J. W. 1983 A class of similarity solutions for the nonlinear thermal conduction problem. *J. Phys. A: Math. Gen.* **16**, 3393–3400.
- MUMLEY, T. E., RADKE, C. J. & WILLIAMS, M. C. 1986 Kinetics of liquid/liquid capillary rise. *J. Colloid Interface Sci.* **109**, 398–425.
- RANSOHOFF, T. C., GAUGLITZ, P. A. & RADKE, C. J. 1987 Snap-off of gas bubbles in smoothly constricted noncircular capillaries. *AIChE J.* **33**, 753–765.
- RANSOHOFF, T. C. & RADKE, C. J. 1988 Laminar flow of a wetting liquid along corners of a predominantly gas-occupied noncircular pore. *J. Colloid Interface Sci.* **121**, 392–401.
- ROLLINS, J. R., GROVE, R. K. & JAEKLE, D. E. JR 1985 Twenty three years of surface tension propellant management system design, development, manufacture, test, and operation. *AIAA Paper* 85-1199.
- SIEGERT, C. E., PETRASH, D. A. & OTTO, E. W. 1964 Time response of liquid-vapor interface after entering weightlessness. *NASA TN D-2458*.
- SINGHAL, A. K. & SOMERTON, W. H. 1970 Two-phase flow through a noncircular capillary at low reynolds numbers. Presented at the 21st Annual Technical Meeting of the Petroleum Society of CIM, Calgary.
- STEEN, P. H. 1996 Capillary and interfacial phenomena, wetting and spreading. In *Research Trend in Fluid Mechanics* (ed. J. L. Lumley et al.), pp. 286–295. AIP Press.
- VERBIST, G., WEAIRE, D. & KRAYNIK, A. M. 1996 The foam drainage equation. *J. Phys.: Condens. Matter* **8**, 3715–3731.
- WEISLOGEL, M. M. 1996 Capillary flow in an interior corner. PhD Thesis, Northwestern Univ.
- WEISLOGEL, M. M. 1997 Spontaneous steady capillary flow in partially coated tubes. *AIChE J.* **43**, 645–654.
- WEISLOGEL, M. M. & LICHTER, S. 1996 A spreading drop in an interior corner: theory and experiment. *Microgravity Sci. Technol.* **IX**(3), 175–184.
- WEISLOGEL, M. M. & ROSS, H. D. 1990 Surface reorientation and settling in cylinders upon step reduction in gravity. *Microgravity Sci. Technol.* **III**(1), 24–32.
- WHITE, F. 1974 *Viscous Fluid Flow*, Chpt. 3. McGraw-Hill.
- WÖLK, G., DREYER, M., RATH H. J. & WEISLOGEL, M. M. 1997 Damped Oscillations of a Liquid/Gas Surface Upon Step Reduction in Gravity. *J. Spacecraft Rockets* **34**, 110–117.
- WONG, H., MORRIS, S. & RADKE, C. J. 1992 Three-dimensional menisci in polygonal capillaries. *J. Colloid Interface Sci.* **148**, 317–336.